Cooperative *cis*-interactions between ectodomains of TCRαβ CD3 subunits enable mechanotransduction

Peiwen Cong[1,2†], Aswin Natarajan[3†], Zhou Yuan[1,2,4,a†], Chenghao Ge[1,2,b†], Stefano Travaglino[1,2], Saikiran Beesam[3], Xiang Li[3], Danielle Grazette[3], Michelle Krogsgaard[3‡], Cheng Zhu[1,2,4‡]

[1]Wallace H. Coulter Department of Biomedical Engineering, [2]Petit Institute for Bioengineering and Bioscience, Georgia Institute of Technology, Atlanta, GA, USA; [3]Laura and Isaac Perlmutter Cancer Center and Department of Pathology, New York University Grossman School of Medicine, New York, NY, USA; [4]Georgia W. Woodruff School of Mechanical Engineering, Georgia Institute of Technology, Atlanta, GA, USA

[†]These authors contributed equally.

[‡]Corresponding authors: Michelle.Krogsgaard@nyulangone.org and cheng.zhu@bme.gatech.edu

[a]Present address: Alfred E. Mann Department of Biomedical Engineering, University of Southern California, Los Angeles, CA 90007, USA

[b]Present address: Amgen Inc., One Amgen Center Dr., Thousand Oaks, CA, USA

ABSTRACT (220 words)

TCR signaling poses a mechanical problem: pMHC binding occurs at the TCRαβ ectodomain (ECD) head, whereas ITAM phosphorylation occurs on CD3 cytoplasmic tails. Chemistry cannot bridge this >10 nm gap, requiring the two events to be coupled through the TCR–CD3 interface, thus involving conformational allostery and being regulatable by force. Although weak ECD *cis*-interactions between TCRαβ and CD3 have been proposed to contribute to this coupling, their kinetics and mechanical competence remain elusive. Here, we quantify TCRαβ–CD3 ECD *cis*-interactions in a pseudo-*cis* configuration using two-dimensional binding and single-bond force spectroscopy, finding that TCRαβ–CD3γε and TCRαβ–CD3δε interactions have low affinity and rapid kinetics, yet form catch bonds. Critically, concurrent engagement of CD3γε and CD3δε produces high *cis*-cooperativity, yielding a stronger and longer-lasting CD3γε–TCRαβ–CD3δε trimolecular catch bond than the sum of the two dimeric bonds, with force-stabilized lifetimes matching those of agonist TCR–pMHC *trans*-interaction. Molecular dynamics simulations reveal an expanded, cooperative, and asymmetric contact network, making CD3δε more force-responsive and susceptible to conformational change than CD3γε. Interface mutations do not alter force-free affinities but remodel cooperative *cis*-bond profiles, leading to an inverse correlation with *trans*-bond profiles and T cell signaling. These results identify cooperative ECD *cis*-interaction as a mechanically regulatable allosteric coupling element at the TCR–CD3 junction important to antigen recognition and signal initiation.

36 **INTRODUCTION** (main text 8207 words)

37 Antigen recognition by the T-cell receptor (TCR) results in T cell activation, leading to
38 proliferation, differentiation, and effector functions (*1*). Signaling is initiated by ligation of
39 peptide-major histocompatibility complex (pMHC) with TCR at its extracellular ligand-binding
40 site, where the antigen information is received, then transmitted across the membrane along the
41 octameric TCR–CD3 complex (TCRαβ associated with CD3γε, CD3δε, and CD3ζζ) to the CD3
42 cytoplasmic tails (*2*). Concurrently, coreceptor CD8 or CD4 places the Src family kinase Lck close
43 to the exposed CD3 tails to phosphorylate their immunoreceptor tyrosine-based activation motifs
44 (ITAMs) (*3*). Phosphorylated ITAMs recruit Zap70, starting downstream signaling cascades (*1, 4*).
45 Despite our detailed knowledge of the structural components of the TCR signaling machinery (*5,*
46 *6*), the mechanism of how pMHC binding at the TCRαβ head leads to phosphorylation of CD3
47 ITAMs, two events separated by ~15 nm in space, precluding the action of local chemistry, remains
48 unclear.

49 Two of the TCR triggering models—conformational change and mechanosensor models (*7-9*)—
50 share a common requirement: a physical coupling pathway must link ligand binding to ITAM
51 phosphorylation. Structurally, this pathway must traverse the interface between TCRαβ and CD3s
52 that includes ectodomains (ECDs), connecting peptides (CP), transmembrane (TM) bundle, and
53 cytoplasmic tails. Yet identifying this coupling has been challenging because the TCR is subject
54 to two seemingly opposing design constraints. On one hand, the complex must be sufficiently
55 connected to maintain quaternary integrity and transmit information. On the other hand, it must
56 remain sufficiently dynamic to permit state transitions that gate signaling. Resolving how
57 molecular architecture balances connectivity with mobility is a central obstacle to a unified
58 physical mechanism of TCR triggering.

59 A likely candidate for this coupling is *cis*-interaction (between proteins anchored to the same cell
60 surface) between the TCRαβ constant domains and the CD3 ECDs. Multiple lines of evidence
61 support this notion: the functional sidedness of CD3s (*10*) and the importance of the TCRαβ
62 constant domains (Cα/Cβ) (*11, 12*) indicate that TCR–CD3 *cis*-interactions are crucial for signal
63 transmission. Disrupting these interactions with anti-CD3 antibodies can change how T cells are
64 activated (*13-15*). The membrane-proximal ECD "ring" may act as the starting point for signal
65 propagation and influences downstream elements such as the CPs (*16*), TM bundle (*17, 18*), and
66 cytosolic tails (*2, 19*). Mutations affecting these *cis*-interactions can impact TCR assembly stability
67 (*20, 21*), surface expression (*22*), down-modulation (*23*), and cellular responses (*10, 21, 24-27*).
68 However, direct mechanistic interpretation has been limited by two gaps. First, ECD interactions
69 appear very weak and transient, raising doubts about their ability to support sustained signal
70 transmission. Second, the subtle coupling may reside in force-dependent dynamic allostery that is
71 sensitive to experimental perturbations, rather than in easily-captured large, stable structural
72 changes, as suggested by discrepant results from different experiments: Early cryo-electron
73 microscopy (cryo-EM) structures (*28-31*) and crosslinking experiments have shown minimal
74 stable rearrangements upon ligation (*27*), whereas nuclear magnetic resonance (NMR) (*32, 33*)
75 and molecular dynamics (MD) (*33, 34*) studies indicate dynamic allostery in the TCR constant
76 domains and at the CD3 interfaces upon pMHC binding.

77 More recent cryo-EM structures of the TCR–CD3 complex reconstituted in nanodiscs suggest
78 unliganded TCR–CD3 adopts "compact/closed" conformations (*35*). Upon pMHC engagement the
79 complex shifts to an "extended/open" architecture, and restricting ECD opening can impair
80 activation (*35*). These findings support the plausibility of activation-linked allosteric transitions,
81 but they do not identify the mechanical mechanism that stabilizes and coordinates this closed-to-

open transition across the TCR–CD3 junction, nor do they establish whether the implicated ECD interfaces are mechanically competent to support TCR–pMHC *trans*-interaction in the presence of force (*1, 6, 18, 36-39*).

Mechanical forces have been suggested to induce conformational allostery (*40-42*), regulate lifetimes of TCR–pMHC *trans*-bonds (*40, 41, 43-46*), and trigger signaling (*43, 47-49*), which, in turn, modulate effector functions (*41, 43, 45, 50, 51*). T cells exert endogenous forces on the TCR–CD3 via engaged pMHC (*52-55*), which must be mediated, at least in part, by TCR–CD3 ECD *cis*-interactions, therefore allowing force to play a role. Thus, mechanical force naturally fits the allosteric framework, likely as a regulator rather than an alternative to allostery. T cells exert forces on engaged ligands, and mechanical load can bias conformational ensembles by stabilizing specific bound states and pathways. In this view, force is a control parameter that can reveal latent allosteric couplings that are otherwise too fleeting to detect at equilibrium. If ECD *cis*-interactions participate in signal transmission, they must satisfy a stringent mechanical criterion: they must remain connected long enough under physiological loads to couple ligand engagement to downstream phosphorylation, while permitting the local rearrangements and fluctuations required for gating. This criterion turns our inquiry into a quantitative question—what are the kinetic and force-dependent properties of the TCRαβ–CD3 ECD *cis*-bonds, and can cooperative assembly transform weak pairwise contacts into a durable, force-stabilized coupling element?

Addressing this question has been difficult because TCRαβ–CD3 ECD *cis*-interactions are too weak and transient to be measured by three-dimensional (3D) methods (*24, 56-58*) such as SPR (Supplementary Fig. 1A, B). Moreover, most prior characterizations have been performed without controlling mechanical load, obscuring whether force reshapes the interaction landscape in ways relevant to mechanotransduction. Thus, despite longstanding hypotheses that ECD *cis*-interactions

105 link antigen recognition to CD3 signaling, direct measurements of their 2D kinetics, cooperativity,
106 and force response have been lacking.

107 Here we combine ultrasensitive biophysical measurements with molecular dynamics (MD)
108 simulations to define the kinetic and mechanical properties of TCRαβ–CD3 ECD *cis*-interactions.
109 Using micropipette adhesion frequency (MAF) assay (*59, 60*) and biomembrane force probe (BFP)
110 thermal fluctuation and force-clamp assays (*43, 61*), we analyzed two-dimensional (2D) binding
111 kinetics of TCRαβ interactions with either CD3γε, CD3δε, or both in a pseudo-*cis* configuration.
112 We find that the bimolecular interactions are low-affinity and short-lived yet form catch bonds,
113 indicating the presence of force-favored bound states. Crucially, co-engagement of CD3γε and
114 CD3δε produces strong synergy in both bond formation and lifetime, resulting in a long-lived
115 cooperative CD3γε–TCRαβ–CD3δε trimolecular catch bond. Complementary analyses at the
116 atomic level using conventional MD (CMD) and steered MD (SMD) simulations corroborate
117 cooperative stabilization through an expanded contact network and reveal asymmetric force
118 responses between CD3γε and CD3δε. Finally, targeted mutations at the trimeric interface remodel
119 force-dependent *cis*-bond profiles without altering force-free affinity, allowing us to relate
120 mechanical coupling at the TCR–CD3 junction to T cell signaling. Together, these results establish
121 cooperative ECD *cis*-interaction as a mechanically regulatable allosteric coupling element that can
122 stabilize and shape information transmission across the TCR–CD3 interface.

123 **RESULTS**

124 **2D kinetic measurements reveal weak TCRαβ–CD3 *cis*-interactions.**

125 To directly measure physical interactions among TCRαβ, CD3γε, and CD3δε (ECDs; hereinafter
126 omitted for simplicity), we utilized the ultra-sensitive MAF assay (*59, 60*) and BFP thermal
127 fluctuation assay (*60, 62*). To compensate for the anticipated low affinities, we coated high
128 densities of hybrid 2B4 TCRαβ (mouse 2B4 TCRαβ variable domains fused with human LC13
129 TCRαβ constant domains) (*26, 63*) and human CD3γε or CD3δε onto opposing surfaces (Fig. 1A,
130 B). To mimic *cis*-interactions, N-terminal biotinylated TCRαβ was coated on one side (*left*), while
131 C-terminal biotinylated CD3s were coated on the opposing side (*right*), allowing head-to-tail
132 alignment for "pseudo-*cis*" contacts. In the MAF assay (Fig. 1A), one red blood cell (RBC) was
133 driven to cyclically contact the other RBC with a consistent contact area (A_c, in μm^2) and time (t_c,
134 in s) and separated to detect binding events from visually observed RBC elongations. An adhesion
135 frequency, P_a (*i.e.*, number of binding events divided by total touches) enumerated from a sequence
136 of repeated contact cycles was measured. Assuming second-order forward and first-order reverse
137 reaction between monomeric TCRαβ and CD3γε or CD3δε, we previously showed that $P_a = 1 -$
138 $\exp(-\langle n \rangle)$, where $\langle n \rangle = m_r m_l A_c K_a [1 - \exp(-k_{off} t_c)]$ is the average number of bonds per
139 contact. Here, m_r and m_l (in μm^{-2}) are the respective densities of TCRαβ and CD3γε or CD3δε,
140 K_a (in μm^2) is 2D affinity, and k_{off} (in s^{-1}) is off-rate (*59, 60*). When $k_{off} t_c \gg 1$, $\exp(-k_{off} t_c) \approx 0$,
141 the effective 2D affinity $A_c K_a$ (in μm^4) can be solved explicitly as $A_c K_a = -\ln(1 - P_a) / m_r m_l$.

142 The effective affinities of TCRαβ–CD3γε and TCRαβ–CD3δε *cis*-interactions were similar (3.78
143 and 2.78 × 10^{-6} μm^4, respectively), which are reliable because they are about an order of magnitude
144 above the detection limit of our current MAF setups (Fig. 1C, *orange* and *blue*) (*46*). For
145 comparison, we measured the 2B4 TCR–K5:IE^k *trans*-interaction side-by-side using the C-

146 terminal biotinylated pMHC-coated RBC to test against the intact TCR–CD3 complex expressed
147 on hybridoma cells. The resulting effective 2D affinity was tens to hundreds of folds higher (~
148 5.87×10^{-4} μm^4, Fig. 1C, *gray*) even though the hybridoma cell surface is rough and the TCRαβ-
149 bearing RBC is smooth, which could result in one to two orders of magnitude lower effective 2D
150 affinity for the rough than smooth cells (*64*). In addition, using C-terminal biotinylated CD3γε and
151 CD3δε coated on the opposing surfaces, we quantified the CD3γε–CD3δε heterotypic interaction
152 (~ 1.10×10^{-5} μm^4, Fig. 1C, *green*), which was higher than the TCR–CD3 heterotypic interactions.
153 Similarly, the effective 2D affinities for the CD3γε–CD3γε, CD3δε–CD3δε, and TCRαβ–TCRαβ
154 homotypic interactions were measured with lower values or undetectable (Supplementary Fig. 1C).

155 To further determine the on- and off-rate, we used the BFP thermal fluctuation assay to measure
156 off-rate, k_{off} (*60, 62*). We attached a functionalized glass bead to the apex of the micropipette-
157 aspirated ultra-soft hypotonic RBC to form the probe on the left (Fig. 1B), whose thermally driven
158 fluctuations were monitored in real time with high spatial-temporal precision (few nanometers and
159 sub-milliseconds) (*65*). The target bead coated with the corresponding binding partner was brought
160 close to the probe to allow molecular contacts via thermal fluctuations, facilitating bond formation.
161 Upon binding, the receptor–ligand (*i.e.*, either TCRαβ *vs.* CD3, CD3 *vs.* CD3, or pMHC *vs.* TCR–
162 CD3) bond acted as an additional spring in parallel with the RBC spring, dampening the confined
163 Brownian motions (*60, 62*). The sudden reduction in thermal fluctuations indicated bond formation,
164 while the restoration to the original fluctuation amplitude marked bond dissociation. The durations
165 in between represent bond lifetimes, which were exponentially distributed, and the reciprocal of
166 the mean bond lifetime is equal to the k_{off}. The 2D off-rates for TCRαβ–CD3γε, TCRαβ–CD3δε,
167 and CD3γε–CD3δε *cis*-interactions measured in this way were very rapid (> 10 s^{-1}) compared to
168 the slower k_{off} of the 2B4 TCR–K5:IE^k *trans*-interaction plotted alongside in Fig. 1D. These

169 results also validated the ~ 2 s contact time used in our MAF assay, which was sufficiently long to
170 ensure the measured adhesion frequencies had reached steady-state. Finally, the effective 2D on-
171 rates, $A_c k_{on}$, were calculated as $A_c k_{on} = A_c K_a \times k_{off}$ for the corresponding interactions (Fig. 1E).
172 Together, the very low affinities and fast off-rates explain why SPR failed to detect these weak and
173 rapid TCRαβ–CD3 interactions, underscoring the ultra-sensitivity of our 2D assays (*66*).

174 **Pairwise *cis*-interactions among TCR–CD3 ECDs form bimolecular catch bonds.**

175 We (*41-44, 46, 50*) and others (*40, 45, 51, 67, 68*) have shown that mechanical force modulates
176 TCR–pMHC *trans*-interactions and amplifies antigen discrimination (*40, 43, 44*). To test whether
177 force also modulates dissociation of the TCR–CD3 *cis*-interactions, we used the BFP force-clamp
178 assay (*41, 43-45*) to measure the force-dependent lifetimes of TCRαβ–CD3γε, TCRαβ–CD3δε,
179 and CD3γε–CD3δε *cis*-bonds (Fig. 1B). Like in the thermal fluctuation assay, we also used bead-
180 mounted RBCs as ultra-sensitive force transducers to measure molecular interactions in the force-
181 clamp assay. Unlike the thermal fluctuation assay, which positioned the target bead at the null
182 position for bond formation and dissociation at zero force, the force-clamp assay retracted the
183 target by a pre-set distance to exert a constant tensile force onto the bond. To enhance stability of
184 force measurement, a dual-edge tracking system was implemented to monitor the positions of both
185 the BFP micropipette and the probe, allowing us to subtract the micropipette drifts from the force
186 signals. The target was programmed to move in repeated "approach-touch-retract-hold-return"
187 cycles, generating a force *vs.* time trace (Fig. 1F) that exemplified both non-binding and binding
188 events. The compressive (negative) force indicates bead-target contact during which bond
189 formation can occur. Upon retraction, the compressive force either returns to zero (no binding) or
190 converts to tensile (positive) force (binding). In the latter case, retraction was halted at the
191 designated force level until bond dissociation, indicated by the sudden return of force to zero.

192 Interestingly, BFP measurements revealed that all three *cis*-interactions formed catch bonds, with
193 mean lifetimes prolonged by low forces (< 7-17 pN, depending on the specific interaction) until
194 being overpowered by higher forces that turned the bond profiles into slip bonds (*i.e.*, mean bond
195 lifetimes shortened by forces, Fig. 1G). These findings demonstrate that TCR–CD3 *cis*-interactions
196 can bear durable force, supporting the notion that information on antigen recognition can be
197 transmitted mechanically through TCRαβ–CD3 interactions.

198 Notably, these TCRαβ–CD3 *cis*-interactions exhibited shorter bond lifetimes across the entire
199 force range than our previously reported TCRαβ–pMHC *trans*-bonds here (replotted from (*42*) in
200 Fig. 1G, *gray*), suggesting that individual TCRαβ–CD3 bimolecular *cis*-interactions alone may not
201 persist long enough to fulfill the proposed mechanical transmission requirements. The 1:1:1
202 stoichiometry of TCRαβ:CD3γε:CD3δε revealed by the cryo-EM structures (*28, 29, 31*) and our
203 direct kinetic measurements of CD3γε–CD3δε interactions (Fig. 1C-E, G, *green*) prompted us to
204 ask: Does TCRαβ bind CD3γε and CD3δε concurrently to form stronger bonds? If so, is this
205 concurrent binding independent or cooperative? If cooperative, how much is the bond stability
206 enhanced, and does this enhancement meet the mechanical transmission requirements?

207 **CD3δε and CD3γε interact with TCRαβ cooperatively in bond formation and bond lifetime.**
208 To test whether CD3δε and CD3γε interact with TCRαβ cooperatively in *cis*, we applied affinity-
209 and lifetime-based measurements with MAF and BFP while co-presenting both CD3s. The results
210 were compared against predictions from a non-cooperative binding model. Significant deviations
211 from these predictions are taken as evidence for positive *cis*-cooperativity.

212 To ensure rigorous comparison of adhesion frequencies, a single TCRαβ-bearing RBC was
213 sequentially brought into contact with a RBC coated with CD3γε, CD3δε, or an equimolar mixture
214 of both (denoted CD3m) in randomized order (Fig. 2A). Streptavidinylated RBCs were prepared

215 from the same batch and coated using excess amounts of biotinylated CD3s to ensure saturated
216 mounting to SA with equivalent density. Adhesion frequencies were measured over 30 touches per
217 pairing for TCRαβ–CD3γε, TCRαβ–CD3δε, and TCRαβ–CD3m (Fig. 2B, connected by *solid lines*)
218 before switching to a new TCRαβ-bearing RBCs (specificity checks of all interactions are shown
219 in Supplementary Fig. 1D). Across eight TCRαβ RBCs tested, the adhesion frequency to CD3m
220 was consistently higher than either subunit alone. To interpret this result, we transformed P_{a} into
221 the average number of bonds per contact, $\langle n \rangle = -\ln(1 - P_{\mathrm{a}})$, which is additive for independent,
222 concurrent binding (*69, 70*). Under this non-cooperative assumption, the predicted bond number
223 for CDm is $\langle \hat{n}_{\mathrm{m}} \rangle = 1/2\langle n_{\gamma\epsilon} \rangle + 1/2\langle n_{\delta\epsilon} \rangle$, where $\langle n_{\gamma\epsilon} \rangle$ and $\langle n_{\delta\epsilon} \rangle$ were measured from respective
224 bimolecular TCRαβ interactions with the single CD3 species indicated by the subscripts (Fig. 2B,
225 *horizontal dotted line*). Strikingly, the observed $\langle n_{\mathrm{m}} \rangle$ significantly exceeded the predicted $\langle \hat{n}_{\mathrm{m}} \rangle$,
226 falsifying the independent binding hypothesis and demonstrating cooperative binding. The degree
227 of cooperativity can be calculated as $\langle n_{\mathrm{m}} \rangle / \langle \hat{n}_{\mathrm{m}} \rangle - 1$, yielding a value of 170%, substantially
228 higher than zero (Fig. 2C), confirming pronounced positive *cis*-cooperativity.

229 Next, we used BFP thermal fluctuation and force-clamp assays to measure the average lifetimes
230 of TCRαβ–CD3m bonds (denoted as τ_{m}) in the absence and presence of force. The BFP target
231 beads were functionalized similarly to the target RBCs in the MAF assay, except that the surface
232 density of TCRαβ was adjusted to maintain infrequent adhesion events (≤ 20%), ensuring a high
233 probability (~ 90%) of single specific bonds (*59*) (Supplementary Fig. 1E-H). The lifetime
234 scattergram was globally fitted by the previously described two-state, two-pathway dissociation
235 models (Supplementary Fig. 2A-I) (*46*). TCRαβ–CD3m bonds persisted significantly longer than
236 single-ligand TCRαβ–CD3γε or TCRαβ–CD3δε bonds across all force levels tested (Fig. 2D;
237 single-ligand curves replotted from Fig. 1G). The τ_{m} *vs.* f curve peaked at ~ 13 pN with a lifetime

238 of ~ 1.5 s, whereas the $\tau_{\gamma\epsilon}$ and $\tau_{\delta\epsilon}$ *vs.* f curves peaked at ~ 7 and 15 pN, respectively, with lower
239 values of ~ 0.6 s for both. Notably, the τ_{m} bond profile exhibited a more pronounced catching
240 behaviour, closely matching that of the TCRαβ–pMHC *trans*-interaction (Fig. 1G, *gray*; peak at ~
241 10 pN with a lifetime ~1.6 s). These results indicate that dual ligands are able to provide sufficient
242 *cis*-stability for mechanotransmission, whereas single ligands are not.

243 To investigate the basis of this prolonged dual-ligand lifetime, we performed survival analysis on
244 bond lifetime distributions (*60, 62, 65*). The survival probability curve of zero-force lifetimes for
245 TCRαβ–CD3m displayed two distinct decay phases, in stark contrast to the log-linear decay
246 observed for single-ligand *cis*-interactions (Fig. 2E). The presence of a slow-decaying
247 subpopulation confirms the existence of the long-lived bond states, bond species, or both.
248 Similar subpopulations of longer-lasting bonds in dual-ligand were also observed in the
249 survival curves of low- and high-force lifetimes (Supplementary Fig. 2J, K). These longer-lived
250 events likely represent trimolecular CD3δε–TCRαβ–CD3γε bonds that substantially prolong τ_{m},
251 and result in positive cooperativity. To quantify this cooperativity in terms of bond lifetime, we
252 calculated the average lifetime of TCRαβ–CD3m bonds as the weighted sum of the bond lifetimes
253 of two bimolecular interactions expected from no cooperativity, $\tau_{\gamma\epsilon}$ and $\tau_{\gamma\epsilon}$, by $\hat{\tau}_{\mathrm{m}} = P_{\gamma\epsilon} \times \tau_{\gamma\epsilon} +$
254 $P_{\delta\epsilon} \times \tau_{\delta\epsilon}$ (Fig. 2D, *dotted curve*), where the bond formation possibilities, $P_{\gamma\epsilon}$ and $P_{\delta\epsilon}$, equal the
255 respective fractions of TCRαβ–CD3γε and TCRαβ–CD3δε bond numbers, $\langle n_{\gamma\epsilon}\rangle/(\langle n_{\gamma\epsilon}\rangle + \langle n_{\delta\epsilon}\rangle)$
256 and $\langle n_{\delta\epsilon}\rangle/(\langle n_{\gamma\epsilon}\rangle + \langle n_{\delta\epsilon}\rangle)$. The assumption of independent binding predicts $\tau_{\mathrm{m}} = \hat{\tau}_{\mathrm{m}}$, but the
257 cooperative analysis, $\Delta\tau/\hat{\tau}_{\mathrm{m}} = (\tau_{\mathrm{m}} - \hat{\tau}_{\mathrm{m}})/\hat{\tau}_{\mathrm{m}}$, revealed ~ 74% to 328% increments in the CD3γε–
258 TCRαβ–CD3δε trimolecular *cis*-bond lifetime over the force range of 0-30 pN (Fig. 2F),
259 highlighting the strong force-enhanced positive cooperativity.

260 **MD simulations corroborate cooperative interaction of CD3γε and CD3δε with TCRαβ.**

261 To corroborate the experimentally observed *cis*-cooperativity, we performed force-free
262 conventional MD (CMD) simulations (*71*) on TCRαβ–CD3γε, TCRαβ–CD3δε, and CD3γε–
263 TCRαβ–CD3δε complexes. The initial full-atomic model of TCR–CD3 ECDs, including the
264 trimeric and dimeric structures (Fig. 3A and Supplementary Fig. 3A), were extracted from the
265 cryo-EM structure (PDB: 6JXR) (*28*). All equilibrated complexes remained bound after 200 ns
266 CMD simulations. Their binding interfaces were analyzed in terms of contact areas (Fig. 3B and
267 Supplementary Fig. 3B) and binding free energies (Fig. 3C and Supplementary Fig. 3C), which
268 were inversely correlated. Using cooperative analyses similar to Fig. 2C, F, we found these two
269 measures also exhibited positive *cis*-cooperativities (Fig. 3D). Because binding affinity, K_{a}, is
270 related to free energy change, ΔE by $K_{\mathrm{a}} \propto \exp(-\Delta E/k_{\mathrm{B}}T)$, where k_{B} is the Boltzmann constant
271 and T is the absolute temperature, these simulations provide independent verification of
272 cooperative 2D affinity measurements.

273 We next simulated force-induced dissociations of TCRαβ–CD3 complexes using steered MD
274 (SMD) (*72*). A pulling force was applied on the TCRαβ N-terminus, while the C-termini of CD3γε,
275 CD3δε or both were anchored (Fig. 3E, *insets* and Supplementary Fig. 4A). To complete
276 simulation within accessible computational timescales, we used relatively high clamping forces
277 (100-200 pN) to accelerate dissociations, which were detected as sudden increases in the minimum
278 distances between TCRαβ and either or both CD3s (Fig. 3E, *curves* and Supplementary Fig. 4B).
279 The times to dissociate ranked as TCRαβ–CD3δε < TCRαβ–CD3γε < CD3γε–TCRαβ–CD3δε.
280 Simulated force effects on times to dissociation (Fig. 3F) were consistent with experimental
281 lifetime trends, following expected slip behaviors beyond 15 pN (Fig. 2D). The trimolecular
282 CD3γε–TCRαβ–CD3δε bonds dissociated at 626, 404, and 233 ns under 150, 175, and 200 pN,

283 respectively, which persisted at least an order of magnitude longer than the two dimeric bonds. To
284 quantify cooperativity, we calculated $\Delta t/\hat{t}_{\delta\gamma}$, which compares observed times to dissociation, $t_{\delta\gamma}$,
285 to the predicted times to dissociation for the non-cooperative trimolecular complex $\hat{t}_{\delta\gamma} = t_{\gamma\epsilon} +$
286 $t_{\delta\epsilon} - t_{\gamma\epsilon}t_{\delta\epsilon}/(t_{\gamma\epsilon} + t_{\delta\epsilon})$, calculated using the TCRαβ–CD3γε and TCRαβ–CD3δε dissociation
287 times, $t_{\gamma\epsilon}$ and $t_{\delta\epsilon}$, respectively. Observed dissociation times exceeded this prediction by from
288 1,200% at 150 pN to 1,900% at 200 pN, demonstrating strong *cis*-cooperativity and mechanical
289 reinforcement (Fig. 3G). Force-ramp SMD simulations on partial and full TCR–CD3 assembles
290 yielded rupture forces in the same order, TCRαβ–CD3δε < TCRαβ–CD3γε < CD3γε–TCRαβ–
291 CD3δε (Supplementary Fig. 4C, D), further confirming the higher stability of the trimolecular
292 complex. Together, complementary experimental and computational approaches demonstrate
293 positive *cis*-cooperativity between CD3δε and CD3γε in their co-binding to TCRαβ.

294 **Structural basis of *cis*-cooperativity quantified by atomic-level contacts.**

295 To elucidate the structural basis of *cis*-cooperativity, we analyzed interface contacts within the
296 TCRαβ–CD3γε, TCRαβ–CD3δε, and CD3γε–CD3δε dimers and compared them with those within
297 the CD3γε–TCRαβ–CD3δε trimer. The contact area sizes were preserved from the dimer to trimer
298 interfaces with only modest alteration upon incorporation of the third subunit. Because CD3γε and
299 CD3δε bind TCRαβ orthogonally with minimal overlap, their combined contact area in the trimer
300 was only slightly smaller than the sum of dimers. This slight steric loss was more than offset by
301 the gain of the CD3γε–CD3δε contact area in the trimer, which substantially increased the total
302 contact area and lowered the binding free energy (Fig. 3B, C), consistent with *cis*-cooperativity.
303 Similarly, we analyzed hydrogen (H) bonds within the TCRαβ–CD3γε, TCRαβ–CD3δε, and
304 CD3γε–CD3δε dimers and compared them with those within the CD3γε–TCRαβ–CD3δε trimer,

305 finding substantially more H-bonds in the trimer than in the dimers at the start and in the middle,
306 but not near the end of SMD simulations (Supplementary Fig. 4E). Similar cooperativity
307 calculations found > 100% and 180% more H-bonds in the trimer without and with force,
308 respectively (Supplementary Fig. 4F).

309 We further quantified the level of interfacial contact using dynamic distances from each residue to
310 its binding partner. We termed this quantification occupancy, defined as the fraction of simulation
311 time during which the center of mass of that residue remains within 4 Å of any atom of the *cis*-
312 interacting ECDs. As such, the occupancy of an individual residue ranks from 0% to 100% as
313 interaction strengthens.

314 To reveal dynamic binding footprints, we mapped these occupancies onto the molecular surfaces,
315 with color intensities proportional to occupancy percentages (Fig. 4A). To expose the respective
316 TCRαβ–CD3γε and TCRαβ–CD3δε interfaces, a pair of the same trimer with different views
317 formed the mirror images, where CD3γε (Fig. 4A, *left*) and CD3δε (Fig. 4A, *right*) were rotated
318 outward away from fixed TCRαβ. Differential color coding was used to indicated CMD-derived
319 occupancy levels on interfaces of CD3γε–TCRαβ–CD3δε trimer (*cyan*), TCRαβ–CD3γε dimer
320 (*magenta*, after CD3δε removal), and TCRαβ–CDδε dimer (*yellow*, after CD3γε removal),
321 respectively. Overlay of dual-color maps (*blueish* overlap for TCRαβ–CD3γε; *greenish* overlap for
322 TCRαβ–CD3δε) highlighted conserved interactions. These analyses revealed the shifts in residue
323 contacts from residing in the respective dimeric structures to the trimeric structure in the absence
324 of force. Interestingly, the interface of TCRαβ with CD3γε was nearly unchanged by the presence
325 of CD3δε (Fig. 4A, *left*, *magenta vs. cyan*), whereas that with CD3δε exhibited a marked
326 reorientation in the presence of CD3γε (Fig. 4A, *right*, *yellow vs. cyan*). This was consistently
327 observed in all three independent CMD runs.

328 To quantify occupancy footprint colocalization between dimer and trimer states, we calculated
329 Manders' overlap coefficients (*73*), finding significantly greater values for CD3γε than CD3δε (Fig.
330 4B). The higher Manders' coefficient for γε than δε revealed a higher level of overlapping contact
331 interfaces between trimer and dimer of TCRαβ with CD3γε than CD3δε, which negatively
332 correlated with the level of contact adjustments going from dimer to trimer after adding the missing
333 CD3. This indicates that, structurally, the TCRαβ–CD3γε interface remains unchanged with or
334 without CD3δε, whereas the TCRαβ–CD3δε interface must reshape to accommodate the
335 incorporation of CD3γε during trimeric assembly. Asymmetric TCRαβ interactions with two CD3s
336 may result in unequal contributions to *cis*-cooperativity.

337 **Asymmetric responses of CD3ε under *cis*-cooperativity and mechanostranmission.**

338 To further elucidate the asymmetric roles of CD3s during cooperative binding and force
339 transmission, we investigated the differential dynamic responses of CD3γε *vs.* CD3δε using
340 occupancy and fluctuation analyses. We first compared the occupancies determined using SMD
341 simulations in the presence of force with values determined in previous section using CMD
342 simulations for every single α, β, γ, ε, δ, and ε' chains (note the omissions of TCR and CD3
343 designations for simplicity). Hereinafter, we use ε' to denote the ε chain that forms the heterodimer
344 with the δ chain to distinguish it from the ε chain that forms the heterodimer with the γ chain,
345 despite their identical sequences. Notwithstanding the average occupancies of ε' and ε chains of
346 the trimer were similar in the absence of force, ε' had far fewer contact residues with αβ than ε
347 both in the absence and presence force, indicating asymmetry (Fig. 4C). Interestingly, under
348 pulling force applied to the TCRαβ, both the number of residues with non-zero values and the
349 domain average of ε' occupancies declined sharply, whereas those of ε remained stable (Fig. 4C).

350 These data suggest that ε' is more sensitive to force, whereas ε provides more mechanical support
351 for *cis*-cooperativity.

352 To expand the ε and ε' occupancy data (Fig. 4C), we similarly calculated mean occupancies of αβ
353 residues contacting γ and δ domains from CMD and SMD simulated γε–αβ–δε trimer. We also
354 performed parallel occupancy calculations using simulated αβ–δε and αβ–γε dimers for all CD3
355 chains. We then plotted these paired occupancies as points using values obtained from CMD
356 (without force) and SMD (with force) as *x*- and *y*-coordinates and drew vectors connecting any
357 two points for the same CD3 chains with the start- and end-point coordinates calculated from
358 simulated dimeric and trimeric structures, respectively (Fig. 4D). The magnitude of a vector
359 represents the amount of occupancy change for a single CD3 chain (γ, ε, δ, or ε') from before (as
360 αβ–γε or αβ–δε dimer) to after (as γε–αβ–δε trimer) incorporating the missing CD3 heterodimer
361 (δε or γε). Remarkably, the δ (*red*) and ε' (*blue*) vectors were of much larger magnitudes than the
362 γ (*green*) and ε (*orange*) vectors, revealing much larger cooperativity-induced occupancy changes
363 in the δ and ε' than the γ and ε chains. This quantitatively depicts the strength of larger non-
364 overlapping trimer and dimer footprints (*cyan areas*) of δε (Fig. 4A, *right*) than γε (Fig. 4A, *left*),
365 re-emphasizing that, to form a γε–αβ–δε trimer via cooperative *cis*-interaction among ECDs, it
366 requires more contact adaptation from incorporating γε into the αβ–δε dimer than incorporating δε
367 into the αβ–γε dimer.

368 The directions of these vectors indicate whether the changes are positive (increasing) or negative
369 (decreasing). Their *x*- and *y*-components represent the changes occurring in the absence and
370 presence of a 175 pN force, respectively. On Fig. 4D, points below (*light blue*) or above (*light red*)
371 the diagonal line indicate domain contacts of αβ with CD3 chains that are suppressed or enhanced
372 by force, respectively. Interestingly, δ switched from a force-suppressed to a slightly force-

373 enhanced state (moving from below to above the diagonal line), while ε' redirected from slightly
374 force-enhanced to force-suppressed (moving from above to below the diagonal line); by
375 comparison, hardly any changes of force-induced contacts, and neither switches of their force-
376 enhanced (γ) and force-suppressed (ε) states were seen in either γ or ε chain. (Fig. 4D). These
377 results reveal that δε is more force-sensitive and γε is more mechanically stable, indicating their
378 different roles in transmitting force across the interfaces between TCRαβ and the two CD3 ECDs

379 In addition to occupancy analysis, which measures contact stability, we analyzed root-mean-square
380 fluctuations (RMSF) in the absence and presence of a 175 pN clamp force, which reflect residue
381 flexibility. By averaging across the entire chain, we assessed the mobility changes of different
382 chains before and after applying force, revealing another layer of mechano-responsiveness for the
383 trimer. ε' showed a larger mean RMSF than ε (Fig. 4E), and force-enhanced RMSF in both ε' and
384 ε residues, but much more for ε' than ε (Fig. 4E). These results inverted the trends of the occupancy
385 data (Fig. 4C), showing a negative correlation expected intuitively. The differences in RMSF
386 values calculated in the presence and absence of force (ΔRMSF) were projected onto the TCR–
387 CD3 quaternary ECD structure, where force-enhanced (*blue*) and force-suppressed (*red*)
388 fluctuations were indicated by color, and absolute ΔRMSF values in response of force were
389 indicated by backbone thickness (Fig. 4F). Under pulling, δε exhibited more amplified dynamics
390 than γε, forming a hinge in δ (*red*) and promoting an out swinging of the semi-detached ε' (*blue*),
391 further revealing asymmetry between γε and δε.

392 **Identifying residues critical to *cis*-cooperativity and their distinctive force-responses.**

393 To pinpoint the structural determinants of *cis*-cooperativity, we developed a modified occupancy
394 analysis (*i.e.*, ΣOccupancy) that integrated occupancies from CMD and SMD simulations,
395 weighted by the number of connections from that residue to all residues in the binder. Briefly,

396 instead of residue-to-domain occupancy, we quantified residue-to-residue occupancy in a matrix
397 format (Supplementary Fig. 5A). Subsequently, we summed over all possible contacts with the
398 interacting domain (Supplementary Fig. 6, *gray*) to account for one-to-many interactions. This
399 approach broadened the dynamic range of detection and identified ~10 and 14% more contacting
400 residues in CMD and SMD, respectively, compared with cryo-EM static structure. We used
401 ΣOccupancy to map the high-contact residues at the TCR–CD3 interface, visualized by sidechain
402 color-coding on the structure, thereby highlighting candidate residues with strong interface
403 connectivity (Fig. 4G).

404 To assess force sensitivity, instead of integrating the CMD and SMD results, we calculated the
405 difference between the CMD- and SMD-derived occupancy matrix (Supplementary Fig. 5B).
406 Summing over by row or column yielded ΔOccupancy, in turn identified force-sensitive residues
407 whose contacts were strengthened (*red*) or weakened (*blue*) by pulling (Supplementary Fig. 6 *red*
408 and *blue*). We mapped these force-sensitive residues on the TCR–CD3 interface by color-coding
409 (Fig. 4H). From a top-down view, force preferentially reduced TCRαβ–CD3γε contacts, whereas
410 TCRαβ–CD3δε contacts were more dynamic. It seems reasonable to suspect that these force-
411 sensitive residues play key roles in mediating force transmission across the TCR–CD3 interface.

412 **Mutating interfacial residues alters catch bond but not affinity of TCRαβ–CD3 interactions.**

413 Among all *cis*-contact residues, two regions of the TCRβ constant domain (Cβ) stood out by their
414 strikingly opposite mechano-responses. Both the CC' loop (residues 182-187) and the Helix 4–F
415 strand segment (residues 221-226) were highly conserved and enriched in high ΣOccupancy
416 residues; however, the CC' loop showed negative ΔOccupancy and the Helix 4–F strand displayed
417 positive ΔOccupancy (Fig. 5A). This suggests that force applied from the TCRβ N-terminus to the

418 Cβ domain elicits residue-specific allostery with opposite effects in adjacent structural regions,
419 moving the CC' loop away from, and the Helix 4–F strand closer to, the CD3s.

420 We targeted the Cβ CC' loop and Helix 4–F strand regions, highlighted on the TCRαβ structure
421 (Fig. 5B), and introduced double-alanine mutations: G182A/K183A (GK), N222A/P223A (NP),
422 and N225A/H226A (NH), made to alter residues with both strong (large ΣOccupancy) and force-
423 sensitive (high absolute ΔOccupancy) contacts. As previously reported (*26*), mutant mouse 2B4
424 TCRαβ chains assembled normally with CD3 chains in transduced hybridoma cells, yet altered T
425 cell activation, measured by interleukin-2 (IL-2) secretion upon co-culture with K5:IE^k expressing
426 CHO cells (Fig. 5C, reformatted IL-2 dose-dependent response curves from Ref. (*26*)). Among
427 these, NP acted as a gain-of-function (GOF) mutation, whereas GK and NH behaved as loss-of-
428 function (LOF) mutations. The IL-2 alterations underscore the functional relevance of TCRαβ–
429 CD3 *cis*-interaction in effectively relaying the ligation signals for downstream T cell activation.

430 To scrutinize how *cis*-interactions regulate signaling propagation, we measured *cis*-interactions
431 between WT and mutant (MT) N-terminally biotinylated 2B4 TCRαβ with C-terminally
432 biotinylated CD3γε, CD3δε, or both. To ensure the 1:1 ratio of CD3γε and CD3δε constructs, we
433 engineered flexible amino acid linkers to covalently tether the two CD3 heterodimers, thereby
434 avoiding heterogeneous CD3 mixtures (*i.e.*, *in vitro* CD3γε–CD3δε, see Methods). Comparing
435 MTs to WT TCRαβ, statistically indistinguishable normalized numbers of bonds were observed
436 for bimolecular interactions with CD3γε (7.52 – 10.94 × 10^{-7} μm^4; Fig. 5D, *first group*) and CD3δε
437 (6.25 – 9.11 × 10^{-7} μm^4; Fig. 5D, *second group*) and much higher but similarly valued were
438 observed for trimolecular interactions with both CD3s (22.75 – 27.82 × 10^{-7} μm^4; Fig. 5D, *third*
439 *group*). The cooperative analysis also revealed similar positive cooperativity measures in WT and
440 MT trimers (Supplementary Fig. 7A). Furthermore, *trans*-interactions between complete WT and

441 MT 2B4 TCR–CD3 complexes expressed on hybridoma cells with C-terminally biotinylated
442 K5:IE^k pMHC reported orders of magnitude higher than *cis*-counterparts but near-identical values
443 with each other (5.59 – 5.87 × 10^{-4} μm^4; Fig. 5D, *fourth group*). These results rule out zero-force
444 kinetics of TCRαβ–CD3 *cis*-interaction and TCR–pMHC *trans*-interaction as a possible reason for
445 the altered T cell activation by the mutations.

446 However, under force, more pronounced kinetic differences emerged in terms of the catch-slip
447 bond. Bond lifetime *vs.* force curves for WT and MT TCRαβs with CD3γε were similar (Fig. 5E);
448 so were those with CD3δε, except for the NP mutation (Fig. 5F), which exhibited a markedly
449 enhanced catch bond. Interestingly, when comparing aganist each other, their force-dependent
450 bond lifetimes demonstrated asymmetry again, as measured by the optimal forces where bond
451 lifetime peaks and the catch bond intensities (a metric summarizing force-dependent bond lifetime
452 changes (*42*)), both showing significantly higher values for four TCRαβ mutants interacting with
453 CD3δε than CD3γε (Supplementary Fig. 7B, C). This validates the results from structural analysis
454 and MD simulations (Fig. 4C-F), confirming that CD3δε is more force-responsive than CD3γε.

455 In the case of co-presenting both CD3s, bond lifetime profiles revealed marked mutational effects
456 (Fig. 5G). Notably, the NH LOF TCRαβ mutant formed exceptionally stable bonds with CD3γε–
457 CD3δε, sometimes exceeding 100 seconds, resulting in an average bond lifetime several-fold
458 longer than the WT TCRαβ. Similarly, the GK LOF mutant exhibited an enhanced catch bond with
459 longer lifetimes across the entire force range, whereas the NP GOF mutant displayed a bond profile
460 resembling WT. Recalling our bond measurements for corresponding *trans*-interactions (Fig. 5H,
461 replotted from Ref. (*42*)), the mutational effects on TCR–pMHC *trans*-interactions and TCRαβ–
462 CD3 ECD *cis*-interaction seem exhibit a reverse correlation: the longer the *cis*-bond, the shorter
463 the *trans*-bond and vice versa.

464 **Correlating *cis*- and *trans*-interactions between TCRαβ and CD3s with T cell signaling.**

465 We next inspected possible correlations between IL-2 secretions (Fig. 5C) and the kinetic measures
466 of the ECD *cis*-interactions of WT and MT TCRαβs with either CD3γε, CD3δε, or both in the
467 absence and presence of force. For bimolecular *cis*-interactions, as expected from their statistically
468 indistinguishable values across each group, the effective 2D affinities (Fig. 5D, *first two groups*)
469 showed poor predictive power for normalized IL-2 AUC, with steep regression slopes and/or low
470 R^2 values (Fig. 6A). Here, the inverse of the slope indicates the sensitivity-of-prediction, and R^2
471 reflects the goodness-of-fit (see Methods). Poor predictive powers for T cell function were
472 similarly observed from lifetimes measured at zero force and optimal force (Fig 5E, F) for both
473 TCRαβ–CD3γε and TCRαβ–CD3δε bimolecular *cis*-bonds (Fig. 6B, *orange and blue*, respectively;
474 Supplementary Fig. 7D). Of note, slightly better correlation with T cell signaling was observed for
475 TCRαβ bonds with CD3δε than CD3γε at both types of lifetime measures, with higher R^2 values
476 and more gradual slopes (Fig. 6B, *dotted vs. solid lines*), potentially because of the differential
477 force-responsiveness.

478 To examine the contribution of cooperativity of the CD3γε–TCRαβ–CD3δε ECD *cis*-interaction
479 to T cell activation, the normalized bond numbers (Fig. 5D, *third group*) and lifetimes at zero force
480 (Fig. 5H, 0 pN) of the trimeric interaction were analyzed, but again found lacks of functional
481 correlations due to their comparable values (Fig. 6C, *red*), similar to their bimolecular counterparts.
482 In contrast to the poor function correlations with the peak lifetime at optimal force of the two
483 bimolecular bonds (Fig. 6B, *solid lines*), a significant reverse correlation was observed between
484 peak lifetime of the cooperative trimolecular bond (Fig. 5H, *optimal force*) and IL-2 production,
485 with a much higher R^2 value and a much flatter slope (Fig. 6C, *black*).

486 The sharp contrast between the differential predictive powers at zero and optimal forces prompted
487 us to analyze the force effect more rigorously by plotting *vs.* IL-2 AUC, the goodness-of-fit and
488 sensitivity-of-prediction based on WT and MT lifetimes under each force, finding that the negative
489 correlation persisted across nearly the entire force range tested (Fig. 6D). Because of the negative
490 correlations, the sensitivity-of-prediction followed the reverse trends of catch bonds, with biphasic
491 behavior most pronounced at optimal force, where force-dependent lifetimes diverged the most
492 between TCR WT and MTs. The Pearson coefficient rapidly approached -1 upon application of
493 force and remained strongly correlated across ~ 5-20 pN. These results underscore a
494 mechanotransduction role of the cooperative trimeric *cis*-catch bond.

495 Since IL-2 produced by T cells expressing these WT and MT TCRs correlates with the peak
496 lifetime of TCR–K5:IE^k *trans*-bonds (*42*), we correlated the peak lifetimes of *trans*- against *cis*-
497 interactions, finding strong anti-correlations with those of the trimer ($R^2 \sim 0.8$, Fig. 6E, *black*), but
498 not dimers ($R^2 < 0.5$, Fig. 6E, *orange* and *blue*). To confirm the force effect on *cis*- and *trans*-
499 coordination, we plotted the force-dependent fitting of *cis*- *vs. trans*- bond profiles for WT and NP,
500 GK, and NH mutants indicated no correlation in the absence of force (Pearson coefficient, $r \sim 0$ at
501 zero force), and weak correlations in the presence of force for the bimolecular *cis*-bonds ($0.33 < r$
502 < 0.73 for γε , and $-0.03 < r < 0.82$ for δε; Supplementary Fig. 7E), but strong negative-correlations
503 in the presence of force for the trimolecular *cis*-bond (r dropped sharply, reaching ~ -1 at 10 pN
504 before rebounding; Fig. 6F). Such correlation analysis reveals an interesting synergy between
505 *trans*- and *cis*-interactions, suggesting a possible feedback mechanism of the TCR
506 mechanosensory machine: from the constant domains, the downstream mechanotransduction
507 region transmitting back to the variable domains, the antigen recognition region.

508

509 **DISCUSSION**

510 Noncovalent *cis*-interactions between the TCRαβ and CD3 chains are essential because they not
511 only hold the octameric TCR–CD3 complex together stably but also provide the "wiring" bridging
512 the >10 nm spatial gap between ligand engagement at the TCRαβ N-termini and ITAM
513 phosphorylation at the CD3 cytoplasmic tails (Supplementary Fig. 8A, *right*). NMR chemical-shift
514 perturbation experiments revealed TCRαβ–CD3γε and TCRαβ–CD3δε ECD dimeric interactions
515 (*26*), but their functional relevance has been difficult to test because these contacts are
516 exceptionally weak and fast. Using MAF and BFP assays that measure direct physical interactions
517 in the same membrane-proximal geometry where these interfaces exist, we quantified the kinetics
518 of TCRαβ–CD3γε and TCRαβ–CD3δε bimolecular binding and CD3γε–TCRαβ–CD3δε
519 trimolecular binding both in the absence and presence of force, showing that these ECD *cis*-
520 interactions are not merely structural accessories but are force-bearing, force-regulated bonds. A
521 key indication that the TCR–CD3 ectodomain junction can function as a mechanically addressable
522 coupling element—capable of transmitting, filtering, and stabilizing information under load rather
523 than simply holding the complex together at rest—is the discovery that these interactions form *cis*-
524 catch bonds (Supplementary Fig. 8A, *left*).

525 However, the individual TCRαβ–CD3γε and TCRαβ–CD3δε bimolecular catch bonds are too
526 short-lived to sustain mechanotransmission over the lifetime of an agonist TCR–pMHC interaction.
527 We showed that the solution to this paradox is cooperativity: When CD3γε and CD3δε engage
528 TCRαβ concurrently, the resulting trimolecular assembly exhibits strong positive *cis*-cooperativity,
529 more likely forming a long-lived *cis*-catch bond whose mechanical stability matches that of the
530 TCR–pMHC *trans*-catch bond (Supplementary Fig. 8B). While early assembly studies suggested
531 *cis*-interaction cooperativity among the TM bundles in the TCR–CD3 intra-complex (*17, 74*) since

532 both CD3γε and CD3δε were required for their enhanced assembly with the TCRαβ (*25*), the
533 present work qualitatively demonstrated and quantitatively evaluated the trimolecular binding
534 cooperativity, using a kinetic approach that follows our previous analysis of positive cooperativity
535 in the TCR–pMHC–CD8 (*50, 75, 76*) and TCR–pMHC–CD4 (*46*) trimolecular interactions, as
536 well as the negative cooperativity between two distinct sets of immuno-*trans*-interactions: TCR–
537 pMHC–CD8 and PD-1–PD-ligands (*77*). Note that our measurements are likely underestimated
538 because the TCR and CD3 ECDs were measured under pseudo-*cis* configurations without TM
539 bundling, which would place them in the most appropriate orientations, especially when CD3γe
540 and CD3δε were captured randomly as CD3m on the beads. In addition to biophysical
541 measurements, CMD and SMD simulations provide multiple lines of corroborative evidence for
542 strong synergy. These include contact areas, free energies, dissociation times, distinct dynamic
543 footprints, and contact residues between the ECDs of TCRαβ and two CD3s separately or
544 concurrently. Regardless of the metrics used, our results definitively demonstrated positive
545 cooperativity in the TCR–CD3 *cis*-interactions, as the integrated response of the complex exceeded
546 that of its individual components. Specifically, the whole trimolecular interaction forms more H
547 bonds with larger footprints and stronger contacts that are mechanically more stable and longer
548 lasting than even the sum of the two bimolecular interactions. Conceptually, cooperativity converts
549 two weak, transient tethers into an integrated "mechanical clutch": force preferentially stabilizes
550 the coupled state, enabling sustained load sharing and extending the time window for downstream
551 signaling to commit (Supplementary Fig. 8B).

552 The ability of the cooperative TCR–CD3 ECD *cis*- catch bond to support force for times that match
553 the lifetime of cognate TCR–pMHC *trans*-catch bond implies their importance in signal relay.
554 This may be significant in light of our current perspectives on the role of the *trans*-catch bond in

555 TCR mechanosensing, which enhances the predictive power for T cell response beyond that of
556 binding affinity in the absence of force (*9, 39, 78*). By comparison, γδTCR–CD3 complexes lack
557 interactions among ECDs with flexible CPs (*79-81*); correspondingly, γδTCR–ligand *trans*-
558 interactions form slip bonds and lack mechanosensing (*12*). This contrast highlights the importance
559 of the cooperative trimolecular *cis*-catch bond revealed here, which must contribute, at least in
560 part, to the "mechanical conduit" with the needed structural connectivity among various αβTCR–
561 CD3 chains important for signaling. Such connectivity must be critical for supporting force,
562 regardless of whether applied externally by pMHC or generated endogenously via CD3 cytosolic
563 tails. An interrelated dual role may be envisioned for the cooperativity-reinforced *cis*-catch bond:
564 First, force does not merely test bond strength; it selects bond state. Catch behavior implies an
565 underlying force-favored bound conformation (or pathway) that is accessed more frequently or
566 stabilized under loads. Second, because the cooperative *cis*-catch bond is maximally stabilized
567 within a defined force regime, the TCR–CD3 junction can act as a "force band-pass filter,"
568 preferentially transmitting signals within the physiological force window and rejecting either
569 insufficient load (no stabilization) or excessive load (slip-driven rupture). In this view, the
570 mechanistic role of *cis*-cooperativity is not simply to strengthen the complex, but to shape how
571 mechanical information is encoded in bond lifetimes and, thus, signaling probability. Therefore,
572 our findings support the TCR mechanotransduction hypothesis (*9, 39*) and are also consistent with
573 the allostery hypothesis (*82*).

574 Further support for this view comes from observed fluctuations that are inversely correlated with
575 the cooperatively enhanced contact stability, consistent with dynamic allostery rather than purely
576 elastic linkages within both TCR and CD3 ECDs. NMR (*32, 33*) and CMD (*33, 41*) studies have
577 observed long-range allosteric communication across the TCRαβ ECD upon ligand engagement,

578 manifesting as chemical shift changes and increased dynamics at the CD3 binding site, suggesting
579 regulatory capacity via distant conformational coupling. Dynamics of CD3s have been
580 hypothesized to be the primary drivers of cross-membrane signal transmission, based on their more
581 structured CP regions compared to the flexible TCR anchors (*83*). Although early cryo-EM (*29,*
582 *30*) and photo-crosslinking (*27*) studies failed to detect a different stable conformation upon pMHC
583 or activating antibody ligation in the absence of force, a recent cryo-EM study observed distinct
584 conformations of the TCR–CD3 complex preserved in native states using nanodiscs (*35*). The
585 conceptual connection is that cooperative *cis*-coupling provides a plausible means to stabilize and
586 mechanically gate such large-scale ECD rearrangements: weak pairwise contacts would be
587 insufficient to sustain coordinated motion, whereas a cooperative *cis*-catch bond could maintain
588 quaternary integrity while allowing force to bias transitions between compact and open ensembles.

589 Consistent with the mechanically regulated dynamic allostery is the asymmetric responses of the
590 two CD3 ECDs, arising from their dissimilar molecular architectures and distinct interactions with
591 the TCR α and β chains (Supplementary Fig. 8A, *right*). The Cβ FG loop has been suggested to be
592 important for TCR mechanosensing, partly because of its proximity to the CD3γ ECD, which may
593 restrict domain motions (*40, 84, 85*). Additionally, CD3δε exhibits heavier glycosylation than
594 CD3γε (*57, 86*), suggesting a tighter association of CD3γε with TCRβ than CD3δε. Here, we found
595 that across SMD and BFP (but not CMD and MAF) measurements, CD3δε is more force-
596 responsive and undergoes greater contact reshaping and fluctuation changes, whereas CD3γε
597 maintains a more invariant interface with TCRαβ and appears mechanically more stable. This
598 division of labor suggests a useful conceptual model: CD3γε behaves as a stabilizing strut that
599 preserves the coupled architecture under load, while CD3δε behaves as a compliant hinge that
600 accommodates force-induced rearrangements. Such asymmetric compliance provides a plausible

601 way to meet two competing requirements of mechanotransduction: the complex must remain
602 connected long enough to transmit load, yet must also remain dynamic enough to permit
603 conformational/dynamical transitions that ultimately gate tail exposure and ITAM phosphorylation.
604 Indeed, the ECD asymmetry revealed here may be related to the structural (*35*) and functional (*87*)
605 differences of CD3 chains during TCR triggering. Our findings shed light on the asymmetric
606 behaviors of ε chains, warranting further investigation: upon TCR–pMHC binding, the
607 cytoplasmic tail of γ-associated ε is kept in a constrained, inactive conformation by binding to the
608 inner leaflet of the plasma membrane, while that of δ-associated ε' is exposed to the cytoplasm,
609 ready to be phosphorylated by Lck to initiate TCR signaling.

610 Mutagenesis was used to perturb the ECD *cis*-bonds within the TCR–CD3 assembly to further
611 elucidate their potential mechanotransduction role. Three double mutations at the TCRαβ constant
612 domains were examined due to the high dynamic contacts of these residues with the CD3s, which
613 also show GOF (NP) and LOF (GK and NH) effects as measured by IL-2 production in antigen-
614 stimulated T hybridoma cells (*26*). Interestingly, none of these mutants altered their effective 2D
615 affinities with either CD3 or the normalized average number of bonds with both CD3s when
616 measured in the absence of force. A similar lack of effect was observed with these mutants for
617 bimolecular catch bonds. The only exception was the NP mutation, which forms a much more
618 pronounced catch bond with CD3δε but not CD3γε. Again, this force-dependent asymmetry may
619 be related to the asymmetric behavior of the two ε cytoplasmic tails, for the more adaptive TCRαβ–
620 CD3δε *cis*-bond may serve as the preferred path of force transmission to enable the larger share of
621 total force through the ε' chain, facilitating the release of its cytoplasmic tail for signal initiation.
622 Hypothetically, the mechanotransmission of information requires the TCR–CD3 complex to have
623 a mechanically integrated architecture with directional constraints, achieved by asymmetric

624 coupling, to allow binding of different ligands to tip the balance among pre-existing states of an
625 energetically metastable structure, enabling force-regulated conformational changes to propagate
626 allosterically. Thus, the Cβ mutants further sharpen the mechanistic picture by separating
627 equilibrium binding from mechanical coupling. Despite leaving force-free *cis*-affinity/bond
628 number largely unchanged, these substitutions remodel the force-dependent lifetime landscape—
629 most prominently for the cooperative trimolecular *cis*-catch bond—demonstrating that the
630 functional lever resides in force-activated dynamics rather than in static affinity. In other words,
631 these mutations tune the mechanical impedance of the TCR–CD3 junction: they alter how the
632 interface redistributes force and stabilizes (or destabilizes) mechanically favored bound states.
633 This also provides a practical design principle: mechanotransduction can be engineered by
634 targeting residues that modulate the "force-response" of *cis*-coupling, without necessarily
635 perturbing antigen recognition chemistry.

636 Surprisingly, the GOF mutation suppressed the trimolecular *cis*-catch bond, whereas both LOF
637 mutations enhanced it. This apparent paradox is explained by our MD simulation results, showing
638 that the GOF mutant enables, whereas the LOF mutants disable the TCRαβ synegistic associations
639 with the CD3γε–CD3δε. These opposing effects enhance and restrict CD3 flexibility, respectively,
640 thereby amplifying and attenuating downstream signaling, correspondingly. Indeed, this
641 explanation is consistent with cryo-EM and crosslinking studies, which show that TCR mutants
642 that strengthen the TCR–CD3 interface paradoxically impair T-cell function (*27*), underscoring
643 the functional relevance of CD3 motions.

644 Previously, we found the same mutations produced a positive correlation between T-cell function
645 and *trans*-bond profile: the GOF mutant TCR (NP) formed a stronger catch bond than WT, whereas
646 the LOF mutants (GK and NH) formed a weaker catch bond or even a slip bond, supporting the

647 predictions from our structural and biophysical model of TCR–pMHC bond profile (*42*). The
648 model suggests that domain stretching, tilting, and rotating near the hinges of the Vα/Vβ and
649 Cα/Cβ domains facilitate *trans*-catch bond formation. A striking finding of the present work is the
650 inverse relationship between the cooperative *cis*-catch bond and T-cell function, together with the
651 anti-correlation between the *cis*- and *trans*-bond profiles (Supplementary Fig. 8C). These trends
652 suggest a tradeoff between internal complex stability and external ligand sensitivity: excessive
653 stabilization of the intra-complex *cis*-junction may "over-clutch" the receptor, restricting the
654 structural compliance that supports optimal *trans*-catch bond formation and antigen discrimination,
655 whereas a more labile *cis*-junction may permit the conformational freedom needed to maximize
656 *trans* mechanosensing—up to the point where connectivity becomes limiting. Thus, the
657 unexpected results from this work actually validate our previous model, for the weaker the *cis*-
658 catch bond, the more flexible the TCR–CD3 complex, the stronger the *trans*-catch bond, and the
659 more potent the T cell function. This view is also consistent with the findings of previous studies,
660 which show that LOF and GOF mutations in TM residues correspond to those that stabilize and
661 destabilize the TCR–CD3 complex, respectively (*18, 88*). We therefore propose that TCR
662 triggering requires not maximal *cis*-stability per se, but a balance between connectivity and
663 mobility, such that force can be transmitted while motion remains permissible.

664

665 **MATERIALS AND METHODS**

666 **Proteins, cells, and antibodies**

667 A biotinylation sequence (GLNDIFEAQKIEWHE) was added to the N-terminus of ECD
668 constructs of 2B4 TCRαβ and the C-terminus of human CD3γε, CD3δε, and CD3γε–CD3δε
669 subunits through PCR. For the single heterodimer CD3γε and CD3δε, a 26-residue peptide linker,
670 C-GSADDAKKDAAKKDDAKKDDAKKDGS-N, was engineered to connect different CD3
671 chains (*89*). For the CD3γε–CD3δε heterodimer–heterodimer, a different 25-residue peptide linker,
672 C-GSSPNSASHSGSAPQTSSAPGSQGS-N, was added to join the two dimers (*90*). Proteins were
673 expressed in One Shot™ *E. coli* BL21 (DE3) (Invitrogen) as insoluble inclusion bodies, refolded,
674 and purified as previously described (*26*). Inclusion bodies for IE^k α (with C-terminal biotinylation
675 sequence) and β chains were produced in One Shot™ *E. coli* BL21 (DE3), refolded with K5
676 peptide (ANERADLIAYFKAATKF), and purified as described previously (*91*). For all proteins,
677 purified fractions were biotinylated using a BirA protein ligase kit (Avidity LLC). The biotinylated
678 proteins were further purified by gel filtration (S200, GE Life Sciences) in PBS (pH 7.4). The
679 proteins were tested for biotinylation efficiency by gel-shift analysis after incubation with excess
680 streptavidin.

681 Mouse $58^{-/-}$ T cell hybridoma cells (*92*) expressing mouse CD3 but not TCRαβ were a generous
682 gift from Dr. Bernard Malissen (Centre d'immunologie de Marseille-Luminy, France). $58^{-/-}$ cells
683 were transfected with mutant mouse 2B4 TCR constructs through retroviral transduction and
684 cultured as described previously (*26*). The transduced cells were stained with PE anti-mouse CD3ε
685 (clone 145-2C11, eBioscience) and allophycocyanin (APC)-conjugated anti-TCRβ (clone H57-
686 597, eBioscience) mAbs, then sorted for dual expression of CD3 and TCR. The sorted cells were
687 expanded for 6 days and quantified for TCR and CD3ε expression.

688 **Flow cytometry and site density**

689 Samples were stained using 10 µg/ml (as indicated below) of antibodies in 100 µl of FACS buffer
690 (PBS or Hanks Ca^{2+}/Mg^{2+} free, 2% FBS, 5 mM EDTA, and 0.1% NaN3) for 30 min at 4 °C.
691 Subsequently, samples were washed twice in 500 µl and then resuspended in 300 µl of FACS
692 buffer. High-performance analysis and sorting were conducted using BD FACSAria™ III, then
693 flow cytometric data were processed using FlowJo™ Software. PE-conjugated anti-mTCRβ (clone
694 H57-597, BD Biosciences), anti-mIE^k (clone 14-4-4S, BD Biosciences), and PE-Cy7-conjugated
695 anti-mCD3ε (clone 145-2C11, BD Biosciences) were used for *trans*-interactions. PE-conjugated
696 anti-mTCR Vα11.1, 11.2 (clone RR8-1, Biolegend), anti-hCD3ε (clone UCHT1, Biolegend),
697 isotype rat IgG2b,κ (clone RTK4530, Biolegend), isotype mouse IgG1,κ (clone MOPC-21,
698 Biolegend) were used for *cis*-interactions.

699 **Micropipette adhesion frequency assay**

700 The MAF assay for measuring 2D affinity has been described previously (*59, 60*). Briefly, human
701 RBCs were isolated from whole blood obtained from healthy donors using a protocol approved by
702 the Institutional Review Board of the Georgia Institute of Technology. RBCs were biotinylated
703 with various concentrations of biotin-X-NHS linker (Millipore/Sigma) to achieve different levels
704 of surface functionalization. Then, the biotinylated RBCs were incubated with a saturating amount
705 of tetrameric streptavidin (Thermo Fisher) and the biotinylated protein of interest for 30 min at
706 room temperature for each step. Based on available biotin sites, the protein was fully coupled to
707 RBCs via biotin-streptavidin-biotin conjugations, and the resulting surface density was quantified
708 by flow cytometry.

709 An experiment chamber was assembled by sandwiching coverslips onto short-edge metal spacers,
710 leaving long-edge gaps open for inserting solutions and reagents. The channel bridging two metal

spaces was created by filling the center space with Leibovitz's L-15 Medium (Gibco) and sealing the solution with mineral oil. The chamber was mounted on the stage of an inverted microscope (a 40×/NA 0.75 objective with a 4× TV tube, Nikon, Eclipse Ti) and imaged at 200 frames per second (Basler, Ace 2). RBCs, beads, and hybridoma cells were loaded into different regions of the channel; the forged micropipettes (Sutter Instrument, P-97) were inserted from each side of the openings to form opposing alignments.

Using suction pressures from the manometer systems, a pair of RBCs (or a RBC and a bead or a hybridoma cell), bearing receptor and ligand, respectively, were captured by two opposing capillary micropipettes (Fig. 1A). The piezo-driven target RBC on the right was brought into contact with the stationary probe RBC on the left in the repeated "approach-contact-retract" testing cycles. Binding *vs.* non-binding events were sampled at a constant contact time and a consistent contact area: upon retraction, RBC elongations reflect binding as 1, and no deformations indicate non-binding as 0. The adhesion frequency ($P_{\mathrm{a}} = \langle s \rangle$) is the mean of the obtained Bernoulli sequence (*i.e.*, $\{s_1, s_2, s_3, \cdots, s_n\}$), in other words, the probability of the occurrence of binding events.

Due to the ultra-low affinities, the *cis*-bond formations are *i.i.d.* and rare. Thus, the probability of forming n bonds obeying the Poisson distribution, $p_n = (\langle n \rangle^n / n!) \exp(-\langle n \rangle)$, with a single parameter, $\langle n \rangle$, the mean number of bonds formed during contact time. As a result, the adhesion frequency is expressed as,

$$P_{\mathrm{a}} = 1 - p_0 = 1 - \exp(-\langle n \rangle). \qquad (1)$$

To further relate the characteristic $\langle n \rangle$ to pairwise *cis*-binding kinetics, we established the kinetic differential equation that is governed by the second-order forward and first-order reverse reactions,

$$\frac{d\langle n\rangle}{dt} = m_{\mathrm{r}} m_{\mathrm{l}} A_{\mathrm{c}} k_{\mathrm{on}} - k_{\mathrm{off}}\langle n\rangle \quad (2)$$

733 , where m_{r} and m_{l} (μm^{-2}) are site densities of receptors and ligands on the RBC surfaces, A_{c} (μm^2)
734 and t (s) are contact area and time; k_{on} (μm^2 s^{-1}) and k_{off} (s^{-1}) are 2D on-rate and off-rate, whose
735 ratio gives 2D affinit $K_{\mathrm{a}} = k_{\mathrm{on}}/k_{\mathrm{off}}$ (μm^2). Clearly, one of Eq. 2 solutions is,

$$\langle n\rangle = m_{\mathrm{r}} m_{\mathrm{l}} A_{\mathrm{c}} K_{\mathrm{a}}[1 - \exp(-k_{\mathrm{off}} t)] \quad (3)$$

736 , whose integration constant is zero, assuming there is no bond initially. Because of the rapid off-
737 rates of *cis*-interactions, the exponential term vanishes at steady-state with a long contact time (2
738 s). As a result, effective 2D affinity $A_{\mathrm{c}} K_{\mathrm{a}}$ can be simply derived from P_{a} by,

$$A_{\mathrm{c}} K_{\mathrm{a}} = \frac{\langle n\rangle}{m_{\mathrm{r}} m_{\mathrm{l}}} = \frac{-\ln(1 - P_{\mathrm{a}})}{m_{\mathrm{r}} m_{\mathrm{l}}}. \quad (4)$$

739 Here, m_{r} and m_{l} were determined by calibrating the mean fluorescence intensity (MFI) of a
740 protein of interest fully stained with a PE-tagged antibody against the MFI of PE quantitation beads
741 (BD Biosciences) by flow cytometry.

742 **Biomembrane force probe (BFP)**

743 The BFP thermal fluctuation (*60, 62*) and force-clamp (*43, 50*) assays for measuring bond lifetime
744 in the absence and presence of force, respectively, have been described in detail previously. Briefly,
745 isolated human RBCs were treated and functionalized to form ultra-sensitive mechanotransducers.
746 Probe RBCs were fully biotinylated with a saturated amount of biotin-PEG-NHS (JenKem), then
747 inflated into hypotonic states by nystatin (ThermoFisher). Next, the probe beads were prepared for
748 dual roles: to attach to the RBCs and to display the protein of interest. In short, streptavidin-
749 maleimide (Sigma) was clicked onto thiol-functionalized glass beads (MPTMS, Thermo Fisher)
750 overnight at 4°C. Afterward, the biotinylated protein-of-interest was partially coupled to the
751 streptavidin beads (90 minutes at room temperature), leaving enough vacancies for RBC

752 attachments through biotin-streptavidin interactions. Lastly, either beads, RBCs, or cells were used
753 as the targets, on which the binding partners were either chemically conjugated or naturally
754 assembled for the probe to test against.

755 A similar experiment chamber (see MAF section) was prepared prior to loading the probe RBCs,
756 probe beads, and targets. In addition to the two opposing micropipettes, a third helper pipette was
757 inserted to assist probe assembly: capturing smaller probe beads and attaching them to the apex of
758 RBCs. The microscope was set up in the same way, but aside from Basler visualization, another
759 high-speed CCD camera (Mako G040B, Allied Vision) was utilized to trace any deformations of
760 the probe RBCs. To do so, a 60-line strip window across the probe was imaged at 1,200 frames
761 per second, where a homemade dual-edge tracking program (LabVIEW, Texas Instruments)
762 scanned the real-time bead positions relative to the reference on the pipette (*i.e.*, the axial length
763 of probe RBCs). This drift-prone design allows ultra-stable and ultra-sensitive micro-
764 manipulations with ~ 2 nm spatial and ~ 1 ms temporal resolutions.

765 1. **Thermal fluctuation assay**

766 This assay is based on the equipartition theorem (*62, 65*), where the RBCs elastic energy is
767 quadratic under small deformations,

$$\frac{1}{2}\kappa_x\langle\Delta x^2\rangle = \frac{1}{2}k_{\mathrm{B}}T \tag{5}$$

768 , where κ_x is the spring constant of RBC's simple harmonic motion, and k_{B} is the Boltzmann
769 constant that scales absolute temperature to energy. The union of the target with the probe, via
770 bond formation, dampens its Brownian motion, equivalent to adding a parallel spring that stiffens
771 the system with a ramped-up spring constant. Whereas bond breakage leads to the restoration of
772 κ_x. Due to the anti-correlation between κ_x and $\langle\Delta x^2\rangle$, the bond association and dissociation events

773 were pinpointed by the sudden decreases and increases in the variance of probe displacements,
774 respectively.
775 During the course of measurements, we adjusted the manometer system to lightly grab the probe
776 RBC using the left micropipette, keeping the RBC ultra-soft with small κ_x to promote sensitive
777 detections. Subsequently, the probe bead was aligned and pushed against the apex of probe RBC,
778 where biotin-streptavidin firmly fused them to assemble the complete mechano-sensing probe (Fig.
779 1b, *left*). Then, we brought the target to the proximity of the probe, leaving a tiny gap between the
780 target's receptor-presenting and the probe bead's ligand-presenting surfaces. Hence, the thermal-
781 driven Δx occasionally closed the gap to allow the ligand-receptor binding. If bonds occurred, the
782 durations between the onsets of $\langle \Delta x^2 \rangle$ reductions and the moments of $\langle \Delta x^2 \rangle$ resumptions (*i.e.*,
783 sequence of events from the exponential random variable, $\{t_1, t_2, t_3, \cdots, t_n\}$) were sampled, whose
784 mean reports the ligand-receptor lifetime, $\tau = \langle t \rangle$. Note that the adhesion frequency was kept low
785 enough to ensure limited second bond formation before breaking the first bond.

786 To calculate the off-rate, k_{off} of pairwise interactions from sampled lifetime events, the kinetic
787 differential equation of first-order reverse reaction is simplified by setting $k_{\text{on}} = 0$ (Eq. 2) as,

$$\frac{d\langle n \rangle}{dt} = -k_{\text{off}} \langle n \rangle. \tag{6}$$

788 Its solution is scalable with the initial number of bonds, $\langle n_0 \rangle$, and reexpressed as the time-
789 dependent survival probability, $P_{\text{s}}(t)$,

$$P_{\text{s}}(t) = \frac{\langle n \rangle}{\langle n_0 \rangle} = \exp(-k_{\text{off}} t). \tag{7}$$

790 As a result, $P_{\text{s}}(t)$, the number of events lasting longer than *t* normalized by total lifetime events,
791 starts from point (0, 1) and decays exponentially. After rearranging lifetime events chronologically,
792 the linear regression slope of survival probability *vs.* time in logarithmic scale estimates k_{off}.

2. Force-clamp assay

The force-clamp assay utilized the same BFP micropipette apparatus, probe setups, and coating strategies as the thermal fluctuation assay (Fig. 1B). Nonetheless, instead of passively monitoring lifetime events without interference, we precisely quantified and interactively manipulated the force levels exerted on the ligand-receptor bonds to obtain the force-dependent lifetime, $\tau(f)$. The probe, as a harmonic oscillator, obeys Hooke's law,

$$f = \kappa_x \Delta x \tag{8}$$

, where κ_x converts the axial displacements into the force applied by the spring. To fine-tune probe stiffness, the suction pressure (Δp) on probe RBCs modulates the hypotonic RBC membrane tension, which, in turn, relates to the spring constant by a geometric scaling factor as,

$$\kappa_x(\Delta p) \approx \frac{2\pi}{\ln\left(\frac{4R_0^2}{R_\mathrm{p}R_\mathrm{c}}\right)}\sigma = \frac{\pi R_\mathrm{p}\Delta p}{\left(1-\frac{R_\mathrm{p}}{R_0}\right)\ln\left(\frac{4R_0^2}{R_\mathrm{p}R_\mathrm{c}}\right)} \tag{9}$$

, where σ is the membrane tension, and the characteristic measures of the probe, R_0, R_p, and R_c, are radii of the outer RBC sphere, the inner RBC cap, and the bead-RBC circular contact, respectively. Typically, the designated Δp sets $\kappa_x \sim 0.3$ pN/nm, which establishes the ultra-sensitive force sensor at a resolution of ± 5 nm in x-deformations.

During experiments, once fine-tuned to the specified stiffness, we utilized a high-precision piezoelectric linear actuator (Physik Instrumente) to micro-manipulate the target, allowing it to undergo "approach-contact-retract-hold-return" testing cycles against the stationary probe. Based on the instantaneous $f(t)$, automated subprograms (LabVIEW, Texas Instruments) made interactive decisions about the target's sub-nanometer movements. The target **approached** the probe till $f(t)$ dropped below zero. Next, the target was stopped at $f(t) \sim -25$ pN and **contacted** the probe

813 to facilitate ligand-receptor associations for a fixed period of ~ 0.5 s. At its end, the piezo **retracted**
814 the target from the probe with two outcomes: a non-binding event was indicated by $\langle f(t)\rangle \sim 0$,
815 and a binding event was detected by $\langle f(t)\rangle \gg 0$ at the moment of separation (Fig. 1F). If the
816 ligand-receptor formed a bond and the ramping-up force reached an expected level, f, the target
817 was **held** in place to maintain the constant Δx, such that the tensile force on the bond was clamped
818 until the spontaneous dissociation occurred (*i.e.*, the sudden decline of $f(t)$). Later, the piezo
819 **returned** the target to its origin to reinitiate the next testing cycle. Among 100s of cycles tested on
820 a pair of targets and probes, lifetime events (*i.e.*, $\{t_1^f, t_2^f, t_3^f, \cdots, t_n^f\}$) were sampled as the time
821 intervals between the instants of $f(t)$ ramped up to the desired magnitudes, and the moments of
822 $f(t)$ suddenly dropped to zero. The mean of lifetime events reports the force-dependent ligand-
823 receptor lifetime, $\tau^f = \langle t^f \rangle$, where the superscript denotes being subjected to the force-clamping
824 of f. To ensure that most interactions represented single-bond events, the site densities of the
825 molecules coated on the beads were adjusted to maintain the adhesion frequency below 20%.

826 **Cooperativity analysis**

827 Multiple metrics were implemented to assess the cooperativity of *cis*-interaction, such as 2D
828 affinity, force-dependent bond lifetime, *etc*. When CD3γε and CD3δε were co-presented, the
829 comparisons between the actual measurements and the expected values assuming independence
830 revealed the level of cooperativity of the TCR and CD3 mixture. To formulate a criterion and a
831 quantitative index for cooperativity, we derived the general form as,

$$\frac{\Delta\langle Y\rangle}{\langle \hat{Y}_{\mathrm{m}}\rangle} = \frac{\langle Y_{\mathrm{m}}\rangle - \langle \hat{Y}_{\mathrm{m}}\rangle}{\langle \hat{Y}_{\mathrm{m}}\rangle} = \frac{\langle Y_{\mathrm{m}}\rangle}{\langle \hat{Y}_{\mathrm{m}}\rangle} - 1 \begin{cases} > 0 & \text{positive cooperativity} \\ = 0 & \text{zero cooperativity} \\ < 0 & \text{negative cooperativity} \end{cases} \tag{10}$$

832 , where Y is an arbitrary random variable about *cis*-interaction, and Y_{m} and $\hat{Y}_{\mathrm{m}}$ are the obtained and
833 expected values from the CD3 mixture, respectively. Zero cooperativity indicates independent

binding, while positive or negative cooperativity signifies dependent binding, with the magnitude of cooperativity quantifying the level of dependency.

Three types of cooperativity analysis were employed to evaluate the *cis*-bindings between TCRαβ and CD3γε, CD3δε mixture using *in vitro* MAF, BFP, and *in silico* SMD dissociation assays. Under the assumption of independent bindings, the expected values for corresponding assays are listed below,

MAF
$$\langle \hat{n}_{\mathrm{m}} \rangle = m_{\alpha\beta} m_{\gamma\epsilon} A_{\mathrm{c}} K_{\mathrm{a}}^{\gamma\epsilon} + m_{\alpha\beta} m_{\delta\epsilon} A_{\mathrm{c}} K_{\mathrm{a}}^{\delta\epsilon} \tag{11}$$

BFP
$$\hat{\tau}_{\mathrm{m}} = \frac{m_{\gamma\epsilon} K_{\mathrm{a}}^{\gamma\epsilon}}{m_{\gamma\epsilon} K_{\mathrm{a}}^{\gamma\epsilon} + m_{\delta\epsilon} K_{\mathrm{a}}^{\delta\epsilon}} \tau_{\gamma\epsilon} + \frac{m_{\delta\epsilon} K_{\mathrm{a}}^{\delta\epsilon}}{m_{\gamma\epsilon} K_{\mathrm{a}}^{\gamma\epsilon} + m_{\delta\epsilon} K_{\mathrm{a}}^{\delta\epsilon}} \tau_{\delta\epsilon} \tag{12}$$

SMD
$$\langle \hat{t}_{\delta\gamma} \rangle = \langle t_{\gamma\epsilon} \rangle + \langle t_{\delta\epsilon} \rangle - \frac{\langle t_{\gamma\epsilon} \rangle \langle t_{\delta\epsilon} \rangle}{\langle t_{\gamma\epsilon} \rangle + \langle t_{\delta\epsilon} \rangle}. \tag{13}$$

Here, K_{a}, τ, and $\langle t \rangle$ in expressions are characteristic kinetic parameters of pairwise *cis*-interactions quantified from corresponding TCRαβ–CD3γε and TCRαβ–CD3δε assays, while A_{c} and m are controllable factors. Note that τ and $\langle t \rangle$ distinguish the quantifications of lifetime using different approaches, where the former population study reports the ensemble average of multiple association states (subscript m), and the latter computer study is based on the single trimeric state (subscript δγ).

Derivations of the expected value of trimeric dissociation lifetime

The expected values for the first two cooperativity analyses are straightforward, and we only show the derivations for Eq. 13 in detail here. The third cooperativity analysis is based on the waiting time of dissociations during SMD simulations. Again, this differs from the population mean of BFP lifetime measurements because we simulated a single-molecular construct at a time, either TCRαβ–CD3γε or TCRαβ–CD3δε, or CD3γε–TCRαβ–CD3δε complexes. Recall that the survival probabilities for the pairwise associations of TCRαβ–CD3γε and TCRαβ–CD3δε are,

$$P_{\mathrm{s}}^{\gamma\epsilon} = \exp\left(-\frac{t}{\langle t_{\gamma\epsilon}\rangle}\right) \text{ and } P_{\mathrm{s}}^{\delta\epsilon} = \exp\left(-\frac{t}{\langle t_{\delta\epsilon}\rangle}\right) \tag{14}$$

, respectively, where $\langle t_{\gamma\epsilon}\rangle$ and $\langle t_{\delta\epsilon}\rangle$ are their corresponding average waiting time till dissociation. Assuming the CD3γε and CD3δε dissociations from the concurrently bound states are independent, and the presence of high loads prevents any rebinding upon dissociations, the cumulative joint probability for TCRαβ to dissociate from both concurrently during (0, *t*) is,

$$F_{\delta\gamma}(t) = \left(1 - P_{\mathrm{s}}^{\gamma\epsilon}(t)\right)\left(1 - P_{\mathrm{s}}^{\delta\epsilon}(t)\right) \tag{15}$$

$$= 1 - e^{-t/\langle t_{\gamma\epsilon}\rangle} - e^{-t/\langle t_{\delta\epsilon}\rangle} + e^{-t\left(1/\langle t_{\gamma\epsilon}\rangle + 1/\langle t_{\delta\epsilon}\rangle\right)}.$$

The corresponding probability density is,

$$\rho_{\delta\gamma}(t) = \frac{dF_{\delta\gamma}(t)}{dt} = \frac{e^{-t/\langle t_{\gamma\epsilon}\rangle}}{\langle t_{\gamma\epsilon}\rangle} + \frac{e^{-t/\langle t_{\delta\epsilon}\rangle}}{\langle t_{\delta\epsilon}\rangle} - \frac{e^{-t\left(1/\langle t_{\gamma\epsilon}\rangle + 1/\langle t_{\delta\epsilon}\rangle\right)}}{1/\langle t_{\gamma\epsilon}\rangle + 1/\langle t_{\delta\epsilon}\rangle}. \tag{16}$$

Thus, the expected value of trimeric dissociation lifetime under the non-coop assumption is,

$$\langle \hat{t}_{\delta\gamma}\rangle = \int_0^\infty t\rho_{\delta\gamma}(t)dt = \langle t_{\gamma\epsilon}\rangle + \langle t_{\delta\epsilon}\rangle - \frac{\langle t_{\gamma\epsilon}\rangle\langle t_{\delta\epsilon}\rangle}{\langle t_{\gamma\epsilon}\rangle + \langle t_{\delta\epsilon}\rangle}. \tag{17}$$

Kinetic modeling of dual-species interaction

To model the dual-species scenario, in addition to the pairwise interactions in the single-species scenario, only the CD3γε–TCRαβ–CD3δε trimolecular interaction is allowed as a concurrent binding state. As such, for simplicity, the total TCRαβ bonds with CD3m include only three subpopulations.

$$\langle n_{\mathrm{m}}\rangle = \langle n_{\gamma\epsilon}^{\mathrm{m}}\rangle + \langle n_{\delta\epsilon}^{\mathrm{m}}\rangle + \langle n_{\delta\gamma}^{\mathrm{m}}\rangle. \tag{18}$$

, where *n* with different subscriptions denote the number of bonds for the TCRαβ–CD3γε, TCRαβ–CD3δε bimolecular interactions, and the CD3γε–TCRαβ–CD3δε trimolecular interaction,

sequentially. Here, the concurrent mode exhibits unique kinetics, redistributing the probabilities of dimeric and trimeric bond formation.

The competitive kinetics between the pairwise and concurrent TCRαβ–CD3s *cis*-interactions follow the two-step model. In the first step, the TCRαβ interacts with either CD3γε (kinetic rates k_1 and k_{-1}) or CD3δε (kinetic rates k_2 and k_{-2}) to form TCRαβ–CD3γε or TCRαβ–CD3δε bimolecular bonds. In the second step, the TCRαβ–CD3δε bond interacts with CD3γε (kinetic rates k_3 and k_{-3}) or the TCRαβ–CD3γε bond interacts with CD3δε (kinetic rates k_4 and k_{-4}) to form CD3γε–TCRαβ–CD3δε trimolecular bonds. Refer to Eq. 2, the modified kinetic differential equations for the steady state are,

$$\frac{d}{dt}\begin{Bmatrix}\langle n^{\mathrm{m}}_{\gamma\epsilon}\rangle\\ \langle n^{\mathrm{m}}_{\delta\epsilon}\rangle\\ \langle n^{\mathrm{m}}_{\delta\gamma}\rangle\end{Bmatrix}+\begin{bmatrix} m_{\delta\epsilon}k_4+k_{-1} & 0 & -k_{-4}\\ 0 & m_{\gamma\epsilon}k_3+k_{-2} & -k_{-3}\\ -m_{\delta\epsilon}k_4 & -m_{\gamma\epsilon}k_3 & k_{-3}+k_{-4}\end{bmatrix}\begin{Bmatrix}\langle n^{\mathrm{m}}_{\gamma\epsilon}\rangle\\ \langle n^{\mathrm{m}}_{\delta\epsilon}\rangle\\ \langle n^{\mathrm{m}}_{\delta\gamma}\rangle\end{Bmatrix}=\begin{Bmatrix} m_{\alpha\beta}m_{\gamma\epsilon}A_{\mathrm{c}}k_1\\ m_{\alpha\beta}m_{\delta\epsilon}A_{\mathrm{c}}k_2\\ 0\end{Bmatrix} \tag{19}$$

, whose solutions are derived as,

$$\langle n^{\mathrm{m}}_{\gamma\epsilon}\rangle=\frac{m_{\alpha\beta}m_{\gamma\epsilon}A_{\mathrm{c}}}{m_{\delta\epsilon}k_4+k_{-1}}\left[k_1+m_{\delta\epsilon}k_{-4}\frac{k_1k_4\left(m_{\gamma\epsilon}k_3+k_{-2}\right)+k_2k_3(m_{\delta\epsilon}k_4+k_{-1})}{k_{-1}k_{-4}\left(m_{\gamma\epsilon}k_3+k_{-2}\right)+k_{-2}k_{-3}(m_{\delta\epsilon}k_4+k_{-1})}\right] \tag{20}$$

$$\langle n^{\mathrm{m}}_{\delta\epsilon}\rangle=\frac{m_{\alpha\beta}m_{\delta\epsilon}A_{\mathrm{c}}}{m_{\gamma\epsilon}k_3+k_{-2}}\left[k_2+m_{\gamma\epsilon}k_{-3}\frac{k_1k_4\left(m_{\gamma\epsilon}k_3+k_{-2}\right)+k_2k_{(45)}(m_{\delta\epsilon}k_4+k_{-1})}{k_{-1}k_{-4}\left(m_{\gamma\epsilon}k_3+k_{-2}\right)+k_{-2}k_{-3}(m_{\delta\epsilon}k_4+k_{-1})}\right] \tag{21}$$

$$\langle n^{\mathrm{m}}_{\delta\gamma}\rangle=m_{\alpha\beta}m_{\gamma\epsilon}m_{\delta\epsilon}A_{\mathrm{c}}\frac{k_1k_4\left(m_{\gamma\epsilon}k_3+k_{-2}\right)+k_2k_3(m_{\delta\epsilon}k_4+k_{-1})}{k_{-1}k_{-4}\left(m_{\gamma\epsilon}k_3+k_{-2}\right)+k_{-2}k_{-3}(m_{\delta\epsilon}k_4+k_{-1})} \tag{22}$$

, where *m* with different subscriptions indicates the site densities of TCRαβ, CD3γε, and CD3δε, respectively.

The cooperativity resides in the second step by allowing the CD3γε–TCRαβ–CD3δε concurrent *cis*-engagements. As expected, letting $k_3=k_4=0$ abolishes the trimolecular bonds and reduces Eq. 20, 21 to the forms of Eq. 3 for the TCRαβ–CD3γε and TCRαβ–CD3δε bimolecular bonds. Note that the comparison between the gain in $\langle n^{\mathrm{m}}_{\delta\gamma}\rangle$ and the loss in $\langle n_{\gamma\epsilon}\rangle-\langle n^{\mathrm{m}}_{\gamma\epsilon}\rangle$ and $\langle n_{\delta\epsilon}\rangle-\langle n^{\mathrm{m}}_{\delta\epsilon}\rangle$

883 defines the sign of cooperativity. Furthermore, the reduction of bimolecular bond fraction leads to
884 the inequality of $\langle n_{\delta\gamma}^{\mathrm{m}} \rangle \geq \Delta\langle n \rangle$. From which, the lower bound for the trimolecular bond fraction
885 can be estimated using solely the value of cooperativity by $\langle n_{\delta\gamma}^{\mathrm{m}} \rangle / \langle n_{\mathrm{m}} \rangle \geq \Delta\langle n \rangle / (\Delta\langle n \rangle + \langle \hat{n}_{\mathrm{m}} \rangle)$(*i.e.*,
886 cooperativity divided by one plus cooperativity). For example, based on the bond number
887 cooperativity of 170% that we measured, the chance of trimolecular bond formation is higher than
888 62% of the total bonds.
889 To model the dual-species dissociation processes, similar to the off-rate analysis in the thermal
890 dynamic assay, by setting the right-hand side of Eq. 19 master equations to zero, we obtained the
891 two-step dissociation of dual-species following a multi-exponential decay. Again, letting the
892 second-step kinetic rates $k_3 = k_{-3} = k_4 = k_{-4} = 0$ reduces the master equations to two
893 uncoupled first-order reverse reactions for the TCRαβ–CD3γε and TCRαβ–CD3δε *cis*-dissociation,
894 following single-exponential decays.

895 **Kinetic modeling of catch-bonds**

896 The *cis*-bond profiles of TCRαβ interacting with CD3γε, CD3δε, or both all demonstrate catch-
897 slip behaviors, with bi-exponential-decay survival probabilities, suggesting the presence of two
898 bound species (*93-95*), particularly under the effects of clamping force. Therefore, for the analysis
899 of force-dependent dissociations of bimolecular bonds, we assumed that a single bond might
900 undergo either a fast-dissociation pathway from a weak state or a slow-dissociation pathway from
901 a strong state (indicated by *), also allowing them to exchange with each other. For the analysis of
902 the mixture bond data, besides combining the two-pathway models obtained for the pairwise
903 TCRαβ–CD3γε and TCRαβ–CD3δε dissociations, we added a third population of trimolecular
904 CD3γε–TCRαβ–CD3δε bonds using the same modeling scheme. The corresponding reaction
905 diagrams for all scenarios are depicted in Supplementary Fig. 2A.

The force dependency of kinetic rates follows Bell's equation (*96*),

$$k_{i,j}(f) = k_{i,j}^{0} \exp\left(\frac{f x_{i,j}}{k_{\mathrm{B}} T}\right) \tag{23}$$

, where the subscript i denotes rates of dissociation along fast (-f) or slow (-s) pathways and of activation into (a) or deactivation from (-a) the strong states; the subscript j denotes different bond types of TCRαβ–CD3γε (γ), TCRαβ–CD3δε (δ), and CD3γε–TCRαβ–CD3δε (δγ); the superscript 0 denotes the respective force-free kinetic rates. According to transition state theory, the force linearly modulates the free energy of the transition barrier, $\Delta E^{\ddagger}(f) = \Delta E_0^{\ddagger} - fx$, and subsequently regulates the kinetic rates, $k(f) = \exp\left(-\left(\Delta E_0^{\ddagger} - fx\right)/k_{\mathrm{B}}T\right)$, werhe x is the characteristic transition distance, and k^0 is proportional to $\exp\left(-\Delta E_0^{\ddagger}\right)$.

This two-state, two-pathway dissociation model (*46*) recapitulated the lifetime of catch bonds and the bi-exponential decay of survival probabilities. Here, the force-free fast dissociation rates for the dimeric bonds were obtained from the thermal fluctuation assay, and the remaining parameters were then evaluated by globally fitting the model to the force-lifetime distributions via maximum likelihood estimation (MLE). The initial proportions of the two states were determined from the ratios of the kinetic rates, assuming equilibrium. A two-step optimization procedure was employed to minimize the MLE: an extensive parameter space was explored using differential evolution to obtain an approximate solution, followed by L-BFGS to hone in on the minimum (Supplementary Fig. 2E-G). The resultant kinetic rates *vs*. force relationships are presented in Supplementary Fig. 2B-D, and Bell's parameters are summarized in Supplementary Table 2. The standard deviation for each parameter was obtained by inverting the Hessian matrix at the MLE to approximate the covariance matrix, whose diagonal entries correspond to the variance of the fitted parameters.

Molecular dynamics simulations

927 **1. Molecular constructs**

928 All simulations were based on the cryo-EM structure (PDB ID: 6JXR) (*28*). The TCRαβ, CD3γε,
929 and CD3δε were truncated near the CPs between extracellular and intracellular regions, leaving
930 the complete TCR–CD3s ECD in its trimeric assembly. The TCRαβ were trimmed at their C-
931 termini, leaving the α-chain Gly22-Glu237 and the β-chain Val26-Glu269. The CD3γε and CD3δε
932 were obtained by truncating the γ-chain after Cys107, ε-chain after Asn121, δ-chain after Glu98,
933 and ε'-chain after Glu124. To minimize potential trimming effects, all chain ends were modified
934 to prevent the exposure of charged residues. An acetyl group was added in front of the N-terminus,
935 and an N-methylamine group capped the C-terminus of every chain. All hydrogen atoms, as well
936 as any missing atoms, were added back through Gromacs utilities (*28*). The disulfide bonds in the
937 original cryo-EM structure were preserved through Gromacs interactive S-S bridge selection
938 procedures (*28*). The resulting CD3γε–TCRαβ–CD3δε trimeric assembly was used to simulate the
939 concurrent *cis*-binding. Then, three partial assemblies were generated to simulate the pairwise *cis*-
940 interactions by removing CD3δε, CD3γε, and TCRαβ individually from the fully-assembled ECDs,
941 yielding dimeric TCRαβ–CD3γε, TCRαβ–CD3δε, and CD3γε–CD3δε, respectively.

942 **2. Unit cell preparation**

943 Unit cells enclosing molecular systems of interest were built with physiologically realistic
944 surroundings and then brought into thermodynamically favorable states. The initial structures were
945 oriented and centered within optimized orthorhombic cells, which accommodated the physical
946 extensions in all directions with a ≥ 1.6 nm buffering zone apart from the box sides to ensure the
947 protein was well-isolated. The molecules in unit cells were solvated using the TIP3P water model
948 (*97*). The negative charges were counterbalanced using sodium ions, and then the ionic strength
949 was set to ~ 150 mM with sodium chloride. To further prepare the system thermodynamically,

energy-unfavorable close contacts were eliminated through the steepest descent and conjugate gradient energy minimization cycles. While restraining the heavy atoms in macromolecules, the unit cell was brought to a suitable ensemble employing a 200-ps velocity rescaling simulation to adjust the temperature and a 200-ps Berendsen Barostat simulation to correct the pressure (300 K, 1.01325 bar). After releasing the heavy-atom restraints, the systems were considered ready for subsequent equilibration and production runs.

3. Conventional molecular dynamics

CMD simulations were performed using GROMACS (version 2019.6) (*98-100*) under the recent AMBER99SB*-ILDNP force field with improved helix-coil transitional and side-chain torsional dynamics (*101*). From previously prepared unit cells, the set of initial velocities was randomly sampled from the Maxwell-Boltzmann distribution. The molecular trajectories were self-evolved under the leap-frog algorithm by integrating Newton's law of motion every 2 fs. For CMD, the individual simulation runs were executed under periodic boundary conditions to sample the NVT ensemble under corresponding constant volumes (*i.e.*, CD3γε–TCRαβ–CD3δε: 12.5 × 10.8 × 9.9 nm^3; TCR–CD3γε: 12.6 × 9.8 × 8.6 nm^3; TCR–CD3δε: 11.9 × 10.3 × 9.2 nm^3; CD3γε–CD3δε: 11.5 × 8.1 × 8.0 nm^3) and 300 K constant temperature. The neighborhood lists were refreshed every 10 steps using the buffered Verlet scheme, with a 1.2 nm non-bonded cutoff for Coulomb and van der Waals interactions. The long-range potentials of electrostatic interactions were computed using the Particle Ewald Mesh summation method. All systems were simulated for 100s ns with three repeats, where each trajectory consists of at least a 50 ns equilibration stage and the remaining production run. Conformational snapshots every 0.1 ns during the production stage were extracted for subsequent analysis.

4. Steered molecular dynamics

973 SMD simulations were initiated from the well-equilibrated configurations from corresponding
974 CMD simulations (*i.e.*, the conformational snapshots at 100 ns). They were prepared according to
975 the Unit cell preparation section, but with a 20-nm box length to accommodate the molecular
976 extension and separation under external pulling. The external forces with constant magnitudes (*i.e.*,
977 force-clamp) or constant velocities (*i.e.*, force-ramp) along the fixed *z*-direction were added to the
978 trimeric and dimeric complexes. The clamping or ramping forces were applied to the N-terminus
979 of the TCRα chain to accelerate the dissociations while keeping the C-termini of CD3ε chains
980 fixed to mimic the anchor effect of their TM domains. For force-clamp simulations, five
981 independent trajectories under 100, 125, 150, 175, and 200 pN were generated for each of the two
982 dimeric systems, but only three independent runs under 150, 175, and 200 pN were executed for
983 the trimeric complex. We aborted the CD3γε–TCRαβ–CD3δε simulations at smaller clamp forces
984 of 100 and 125 pN due to the inability to observe dissociation events after the exceedingly long
985 waiting time (> 1000 ns). For force-ramp simulations, a 70 pN/nm pseudo spring was utilized to
986 exert increasing levels of pulling to accelerate dissociations. One end of the spring was linked to
987 the α chain N-terminus of the targeting molecule, and the other free end departed in the *z*-direction
988 at 1 nm/ns. Five repeats each for two dimeric and one trimeric ECD complexes were performed to
989 assess the corresponding rupture forces as a consistency check.

990 **Occupancy analysis**

991 Several variations of occupancy analysis were employed to dynamically evaluate the extent of a
992 particular residue in dynamic contact with its binding partner throughout the simulation. At
993 timestamp i, the residue being analyzed is defined to be in contact (denoted $o_i = 1$) if the center
994 of mass of this residue is within 4 Å of any atoms of its binding partner; otherwise, it is not in

touch (denoted $o_i = 0$). The occupancy index (%) indicates the fraction of time in contact during a given period, as $\sum_i o_i/N$, where N is the total number of analyzed frames.

1. **Residue-to-residue occupancy** (Supplementary Fig. 5)

By setting residues within a subunit as a reference group, this occupancy analysis quantifies the extent of dynamic interaction between each residue from one subunit and every single residue from the other subunit over a given period. Thus, it evaluated the level of any pairwise contacts, thereby forming a correlation matrix where the column indexes the residues from one subunit; the row indexes the residues from the other subunit, and the elements denote the values of residue-to-residue relative binding strength, ranging from 0 to 1.

1. **Residue-to-domain occupancy** (Supplementary Fig. 6)

This occupancy analysis quantifies each residue against all residues within its binding partner, using the entire subunit as the reference group. It is usually smaller than the sum of residue-to-residue occupancy over the binding domain because the residue in question may simultaneously be in contact with multiple residues in the domain under consideration; on the other hand, these contact periods can only be counted once for residue-to-domain occupancy. To account for this disadvantage, ΣOccupancy is defined as the integration of the CMD and SMD row-/column-wise sums of residue-to-residue occupancies; while ΔOccupancy is defined as the differentiation of the CMD from the SMD row-/column-wise sums of residue-to-residue occupancies, which were calculated to summarize and discriminate force-free and force-clamp interface dynamics (Fig. 4G, H).

2. **Domain-to-domain occupancy**

This occupancy analysis further reduces data presentation to examine the overall binding tendency against the other domain by averaging over all interacting residues (*i.e.,* positive terms of residue-to-domain occupancies), providing a measure of the overall domain-to-domain adhesion strength.

Linear regression

Linear regression was conducted to assess the correlations between *cis*-kinetic measures (as x) and functional outputs or *trans*-kinetic measures (as y). The goodness-of-fit was quantified using Pearson's correlation coefficient, *i.e.*, $(n\sum xy - \sum x \sum y)/\sqrt{(n\sum x^2 - (\sum x)^2)(n\sum y^2 - (\sum y)^2)}$, which preserves the sign of correlation, as well as its square, R-squared. The sensitivity-of-prediction, *i.e.*, $(n\sum x^2 - (\sum x)^2)/(n\sum xy - \sum x \sum y)$, is the inverse of the linear-regression slope.

1026 **ACKNOWLEDGEMENTS**

1027 This work was supported by NIH grants R01GM124489 (to M.K.) and R01CA284604 (to M.K.
1028 and C.Z.) and U01 CA214354 (to C.Z. and M.K.). The MD simulations were supported by an NSF
1029 award MCA08X014 (to C.Z.) in advanced computing infrastructure for the U.S. and performed in
1030 the Extreme Science and Engineering Discovery Environment (XSEDE). Cell sorting/flow
1031 cytometry technologies were provided by NYU Langone's Cytometry and Cell Sorting
1032 Laboratory, which is supported in part by NIH grant P30CA016087. SIYR:H2-K^b protein was
1033 made by the NIH Tetramer Core Facility at Emory University. We thank Larissa Doudy for
1034 technical assistance, Johannes Huppa for providing the H57 scFv, and Bernard Malissen for
1035 providing mouse $58^{-/-}$ T cell hybridoma cells.

1036 **AUTHOR CONTRIBUTIONS**

1037 C.Z., P.C., and C.G. conceived the study; C.Z. and M.K. directed the study; P.C., Z.Y., C.G., and
1038 A.N. performed experiments; P.C. performed simulations; P.C. and A.N. performed structural
1039 analysis; A.N., S.B, and D.G produced proteins; P.C. and S.T. analyzed data using mathematical
1040 models; P.C., A.N., Z.Y., M.K., and C.Z. analyzed data and wrote the paper with contributions
1041 from other authors.

1042 **STATEMENT OF COMPETING INTERESTS**

1043 The authors declare no competing interests. M.K. serves on the scientific advisory boards of
1044 Genentech and Merck and Co. and received research support from Merck Sharp & Dohme Corp.,
1045 a subsidiary of Merck and Co., Inc., Genentech, Biogen, Novartis, and the Mark Foundation.

1046

1047

1048 REFERENCES

1049

1050 1. A. H. Courtney, W. L. Lo, A. Weiss, TCR Signaling: Mechanisms of Initiation and
1051 Propagation. *Trends Biochem Sci* **43**, 108–123 (2018).

1052 2. C. Xu *et al.*, Regulation of T cell receptor activation by dynamic membrane binding of the
1053 CD3epsilon cytoplasmic tyrosine-based motif. *Cell* **135**, 702–713 (2008).

1054 3. L. A. Pitcher, N. S. C. van Oers, T-cell receptor signal transmission: who gives an ITAM?
1055 *Trends in Immunology* **24**, 554–560 (2003).

1056 4. B. Malissen, P. Bongrand, Early T Cell Activation: Integrating Biochemical, Structural,
1057 and Biophysical Cues. *Annual Review of Immunology* **33**, 539–561 (2015).

1058 5. K. C. Garcia, L. Teyton, I. A. Wilson, Structural basis of T cell recognition. *Annual Review*
1059 *of Immunology* **17**, 369–397 (1999).

1060 6. R. A. Mariuzza, P. Agnihotri, J. Orban, The structural basis of T-cell receptor (TCR)
1061 activation: An enduring enigma. *J Biol Chem* **295**, 914–925 (2020).

1062 7. M. Wieczorek *et al.*, Major Histocompatibility Complex (MHC) Class I and MHC Class
1063 II Proteins: Conformational Plasticity in Antigen Presentation. *Frontiers in Immunology* **8**,
1064 (2017).

1065 8. N. Jeffreys, J. M. Brockman, Y. Zhai, D. E. Ingber, D. J. Mooney, Mechanical forces
1066 amplify TCR mechanotransduction in T cell activation and function. *Applied Physics*
1067 *Reviews* **11**, 011304 (2024).

1068 9. S. Travaglino, Y. Jeon, Y. Kim, C. Zhu, H.-K. Choi, Mechanotransduction through T cell
1069 receptor: consensus, controversies, and future outlooks. *Experimental & Molecular*
1070 *Medicine*, (2025 In press).

1071 10. M. S. Kuhns *et al.*, Evidence for a functional sidedness to the alphabetaTCR. *Proc Natl*
1072 *Acad Sci U S A* **107**, 5094–5099 (2010).

1073 11. Elaine P. Dopfer *et al.*, The CD3 Conformational Change in the γδ T Cell Receptor Is Not
1074 Triggered by Antigens but Can Be Enforced to Enhance Tumor Killing. *Cell Reports* **7**,
1075 1704–1715 (2014).

1076 12. R. J. Mallis *et al.*, Molecular design of the γδT cell receptor ectodomain encodes
1077 biologically fit ligand recognition in the absence of mechanosensing. *Proceedings of the*
1078 *National Academy of Sciences* **118**, e2023050118 (2021).

1079 13. J. P. Van Wauwe, J. G. Goossens, P. C. Beverley, Human T lymphocyte activation by
1080 monoclonal antibodies; OKT3, but not UCHT1, triggers mitogenesis via an interleukin 2-
1081 dependent mechanism. *The Journal of Immunology* **133**, 129–132 (1984).

1082 14. S. R. Riddell, P. D. Greenberg, The use of anti-CD3 and anti-CD28 monoclonal antibodies
1083 to clone and expand human antigen-specific T cells. *Journal of Immunological Methods*
1084 **128**, 189–201 (1990).

1085 15. A. P. Menon *et al.*, Modulating T Cell Responses by Targeting CD3. *Cancers*. 2023
1086 (10.3390/cancers15041189).

1087 16. Y. Wang *et al.*, A Conserved CXXC Motif in CD3ε Is Critical for T Cell Development and
1088 TCR Signaling. *PLOS Biology* **7**, e1000253 (2009).

1089 17. M. E. Call, J. Pyrdol, M. Wiedmann, K. W. Wucherpfennig, The Organizing Principle in
1090 the Formation of the T Cell Receptor-CD3 Complex. *Cell* **111**, 967–979 (2002).

1091 18. A. L. Lanz *et al.*, Allosteric activation of T cell antigen receptor signaling by quaternary
1092 structure relaxation. *Cell Rep* **36**, 109375 (2021).

1093 19. K. N. Brazin *et al.*, The T Cell Antigen Receptor α Transmembrane Domain Coordinates
1094 Triggering through Regulation of Bilayer Immersion and CD3 Subunit Associations.
1095 *Immunity* **49**, 829–841.e826 (2018).

1096 20. Z.-Y. J. Sun, K. S. Kim, G. Wagner, E. L. Reinherz, Mechanisms Contributing to T Cell
1097 Receptor Signaling and Assembly Revealed by the Solution Structure of an Ectodomain
1098 Fragment of the CD3ϵγ Heterodimer. *Cell* **105**, 913–923 (2001).

1099 21. N. Martinez-Martin *et al.*, Cooperativity between T cell receptor complexes revealed by
1100 conformational mutants of CD3epsilon. *Sci Signal* **2**, ra43 (2009).

1101 22. R. A. Fernandes *et al.*, T cell receptors are structures capable of initiating signaling in the
1102 absence of large conformational rearrangements. *J Biol Chem* **287**, 13324–13335 (2012).

1103 23. H. Liu, M. Rhodes, D. L. Wiest, D. A. A. Vignali, On the Dynamics of TCR:CD3 Complex
1104 Cell Surface Expression and Downmodulation. *Immunity* **13**, 665–675 (2000).

1105 24. M. S. Kuhns, M. M. Davis, Disruption of extracellular interactions impairs T cell receptor-
1106 CD3 complex stability and signaling. *Immunity* **26**, 357–369 (2007).

1107 25. Y. He *et al.*, Identification of the Docking Site for CD3 on the T Cell Receptor beta Chain
1108 by Solution NMR. *J Biol Chem* **290**, 19796–19805 (2015).

1109 26. A. Natarajan *et al.*, Structural Model of the Extracellular Assembly of the TCR-CD3
1110 Complex. *Cell Rep* **14**, 2833–2845 (2016).

1111 27. A. Natarajan *et al.*, In situ cell-surface conformation of the TCR-CD3 signaling complex.
1112 *EMBO reports* **25**, 5719–5742–5742 (2024).

1113 28. D. Dong *et al.*, Structural basis of assembly of the human T cell receptor-CD3 complex.
1114 *Nature* **573**, 546–552 (2019).

1115 29. L. Sušac *et al.*, Structure of a fully assembled tumor-specific T cell receptor ligated by
1116 pMHC. *Cell* **185**, 3201–3213.e3219 (2022).

1117 30. K. Saotome *et al.*, Structural analysis of cancer-relevant TCR-CD3 and peptide-MHC
1118 complexes by cryoEM. *Nature Communications* **14**, 2401 (2023).

1119 31. Y. Chen *et al.*, Cholesterol inhibits TCR signaling by directly restricting TCR-CD3 core
1120 tunnel motility. *Mol Cell* **82**, 1278–1287 e1275 (2022).

1121 32. K. Natarajan *et al.*, An allosteric site in the T-cell receptor Cbeta domain plays a critical
1122 signalling role. *Nat Commun* **8**, 15260 (2017).

1123 33. S. Rangarajan *et al.*, Peptide-MHC (pMHC) binding to a human antiviral T cell receptor
1124 induces long-range allosteric communication between pMHC- and CD3-binding sites. *J*
1125 *Biol Chem* **293**, 15991–16005 (2018).

1126 34. B. Knapp, P. A. van der Merwe, O. Dushek, C. M. Deane, MHC binding affects the
1127 dynamics of different T-cell receptors in different ways. *PLoS Comput Biol* **15**, e1007338
1128 (2019).

1129 35. R. Q. Notti *et al.*, The resting and ligand-bound states of the membrane-embedded human
1130 T-cell receptor–CD3 complex. *Nature Communications* **16**, 10996 (2025).

1131 36. B. Alarcon, D. Gil, P. Delgado, W. W. Schamel, Initiation of TCR signaling: regulation
1132 within CD3 dimers. *Immunol Rev* **191**, 38–46 (2003).

1133 37. P. A. van der Merwe, O. Dushek, Mechanisms for T cell receptor triggering. *Nat Rev*
1134 *Immunol* **11**, 47–55 (2011).

1135 38. D. Moogk, A. Natarajan, M. Krogsgaard, T cell receptor signal transduction: affinity, force
1136 and conformational change. *Curr Opin Chem Eng* **19**, 43–50 (2018).

1137 39. C. Zhu, W. Chen, J. Lou, W. Rittase, K. Li, Mechanosensing through immunoreceptors.
1138 *Nat Immunol* **20**, 1269–1278 (2019).

1139 40. D. K. Das *et al.*, Force-dependent transition in the T-cell receptor beta-subunit
1140 allosterically regulates peptide discrimination and pMHC bond lifetime. *Proc Natl Acad*
1141 *Sci U S A* **112**, 1517–1522 (2015).

1142 41. P. Wu *et al.*, Mechano-regulation of Peptide-MHC Class I Conformations Determines TCR
1143 Antigen Recognition. *Mol Cell* **73**, 1015–1027 e1017 (2019).

1144 42. H.-K. Choi *et al.*, Catch bond models may explain how force amplifies TCR signaling and
1145 antigen discrimination. *Nature Communications* **14**, 2616 (2023).

1146 43. B. Liu, W. Chen, B. D. Evavold, C. Zhu, Accumulation of dynamic catch bonds between
1147 TCR and agonist peptide-MHC triggers T cell signaling. *Cell* **157**, 357–368 (2014).

1148 44. J. Hong *et al.*, Force-Regulated In Situ TCR-Peptide-Bound MHC Class II Kinetics
1149 Determine Functions of CD4+ T Cells. *J Immunol* **195**, 3557–3564 (2015).

1150 45. L. V. Sibener *et al.*, Isolation of a Structural Mechanism for Uncoupling T Cell Receptor
1151 Signaling from Peptide-MHC Binding. *Cell* **174**, 672–687 e627 (2018).

1152 46. M. N. Rushdi *et al.*, Cooperative binding of T cell receptor and CD4 to peptide-MHC
1153 enhances antigen sensitivity. *Nat Commun* **13**, 7055 (2022).

1154 47. S. T. Kim *et al.*, The alphabeta T cell receptor is an anisotropic mechanosensor. *J Biol*
1155 *Chem* **284**, 31028–31037 (2009).

1156 48. S. Pryshchep, V. I. Zarnitsyna, J. Hong, B. D. Evavold, C. Zhu, Accumulation of serial
1157 forces on TCR and CD8 frequently applied by agonist antigenic peptides embedded in
1158 MHC molecules triggers calcium in T cells. *J Immunol* **193**, 68–76 (2014).

1159 49. Y. Feng *et al.*, Mechanosensing drives acuity of alphabeta T-cell recognition. *Proc Natl*
1160 *Acad Sci U S A* **114**, E8204–E8213 (2017).

1161 50. J. Hong *et al.*, A TCR mechanotransduction signaling loop induces negative selection in
1162 the thymus. *Nat Immunol* **19**, 1379–1390 (2018).

1163 51. A. Akitsu *et al.*, Parsing digital or analog TCR performance through piconewton forces.
1164 *Science Advances* **10**, eado4313 (2024).

1165 52. W. Chen, C. Zhu, Mechanical regulation of T-cell functions. *Immunological Reviews* **256**,
1166 160–176 (2013).

1167 53. K. H. Hu, M. J. Butte, T cell activation requires force generation. *Journal of Cell Biology*
1168 **213**, 535–542 (2016).

1169 54. J. Gohring *et al.*, Temporal analysis of T-cell receptor-imposed forces via quantitative
1170 single molecule FRET measurements. *Nat Commun* **12**, 2502 (2021).

1171 55. D. L. Harrison, Y. Fang, J. Huang, T-Cell Mechanobiology: Force Sensation, Potentiation,
1172 and Translation. *Frontiers in Physics* **Volume 7 - 2019**, (2019).

1173 56. J. Wang *et al.*, Atomic structure of an alphabeta T cell receptor (TCR) heterodimer in
1174 complex with an anti-TCR fab fragment derived from a mitogenic antibody. *EMBO J* **17**,
1175 10–26 (1998).

1176 57. Z.-Y. J. Sun *et al.*, Solution structure of the CD3εδ ectodomain and comparison with
1177 CD3εγ as a basis for modeling T cell receptor topology and signaling. *Proceedings of the*
1178 *National Academy of Sciences* **101**, 16867–16872 (2004).

1179 58. W. Wang *et al.*, Quantitative Analysis of T Cell Receptor Complex Interaction Sites Using
1180 Genetically Encoded Photo-Cross-Linkers. *ACS Chemical Biology* **9**, 2165–2172 (2014).

1181 59. S. E. Chesla, P. Selvaraj, C. Zhu, Measuring two-dimensional receptor-ligand binding
1182 kinetics by micropipette. *Biophys J* **75**, 1553–1572 (1998).

1183 60. J. Huang *et al.*, The kinetics of two-dimensional TCR and pMHC interactions determine
1184 T-cell responsiveness. *Nature* **464**, 932–936 (2010).

1185 61. E. Evans, K. Ritchie, R. Merkel, Sensitive force technique to probe molecular adhesion
1186 and structural linkages at biological interfaces. *Biophys J* **68**, 2580–2587 (1995).

1187 62. W. Chen, E. A. Evans, R. P. McEver, C. Zhu, Monitoring receptor-ligand interactions
1188 between surfaces by thermal fluctuations. *Biophys J* **94**, 694–701 (2008).

1189 63. E. W. Newell *et al.*, Structural basis of specificity and cross-reactivity in T cell receptors
1190 specific for cytochrome c-I-E(k). *J Immunol* **186**, 5823–5832 (2011).

1191 64. T. E. Williams, S. Nagarajan, P. Selvaraj, C. Zhu, Quantifying the Impact of Membrane
1192 Microtopology on Effective Two-dimensional Affinity*210. *Journal of Biological*
1193 *Chemistry* **276**, 13283–13288 (2001).

1194 65. W. Chen, V. I. Zarnitsyna, K. K. Sarangapani, J. Huang, C. Zhu, Measuring Receptor–
1195 Ligand Binding Kinetics on Cell Surfaces: From Adhesion Frequency to Thermal
1196 Fluctuation Methods. *Cellular and Molecular Bioengineering* **1**, 276–288 (2008).

1197 66. B. Liu *et al.*, 2D TCR-pMHC-CD8 kinetics determines T-cell responses in a self-antigen-
1198 specific TCR system. *Eur J Immunol* **44**, 239–250 (2014).

1199 67. X. Zhao *et al.*, Tuning T cell receptor sensitivity through catch bond engineering. *Science*
1200 **376**, eabl5282 (2022).

1201 68. R. Qin *et al.*, TCR catch bonds nonlinearly control CD8 cooperation to shape T cell
1202 specificity. *Cell Research* **35**, 265–283 (2025).

1203 69. C. Zhu, T. E. Williams, Modeling concurrent binding of multiple molecular species in cell
1204 adhesion. *Biophys J* **79**, 1850–1857 (2000).

1205 70. T. E. Williams, P. Selvaraj, C. Zhu, Concurrent binding to multiple ligands: kinetic rates
1206 of CD16b for membrane-bound IgG1 and IgG2. *Biophys J* **79**, 1858–1866 (2000).

1207 71. M. Karplus, G. A. Petsko, Molecular dynamics simulations in biology. *Nature* **347**, 631–
1208 639 (1990).

1209 72. S. Izrailev *et al.*, in *Computational molecular dynamics: challenges, methods, ideas*.
1210 (Springer, 1999), pp. 39–65.

1211 73. E. M. M. Manders, J. Stap, G. J. Brakenhoff, R. V. Driel, J. A. Aten, Dynamics of three-
1212 dimensional replication patterns during the s-phase, analysed by double labelling of dna
1213 and confocal microscopy. *Journal of Cell Science* **103**, 857–862 (1992).

1214 74. N. Manolios, F. Letourneur, J. S. Bonifacino, R. D. Klausner, Pairwise, cooperative and
1215 inhibitory interactions describe the assembly and probable structure of the T-cell antigen
1216 receptor. *EMBO J* **10**, 1643–1651 (1991).

1217 75. N. Jiang *et al.*, Two-Stage Cooperative T Cell Receptor-Peptide Major Histocompatibility
1218 Complex-CD8 Trimolecular Interactions Amplify Antigen Discrimination. *Immunity* **34**,
1219 13–23 (2011).

1220 76. B. Liu *et al.*, The cellular environment regulates in situ kinetics of T-cell receptor
1221 interaction with peptide major histocompatibility complex. *European Journal of*
1222 *Immunology* **45**, 2099–2110 (2015).

1223 77. K. Li *et al.*, PD-1 suppresses TCR-CD8 cooperativity during T-cell antigen recognition.
1224 *Nat Commun* **12**, 2746 (2021).

1225 78. H. K. Choi, C. Zhu, Catch Bonds in Immunology. *Annu Rev Immunol* **43**, 641–666 (2025).

1226 79. W. Xin *et al.*, Structures of human γδ T cell receptor–CD3 complex. *Nature* **630**, 222–229
1227 (2024).

1228 80. B. S. Gully *et al.*, Structure of a fully assembled γδ T cell antigen receptor. *Nature* **634**,
1229 729–736 (2024).

1230 81. M. Hoque *et al.*, Structural characterization of two γδ TCR/CD3 complexes. *Nature*
1231 *Communications* **16**, 318 (2025).

1232 82. B. Alarcon, W. W. Schamel, Allosteric Changes Underlie the Outside-In Transmission of
1233 Activatory Signals in the TCR. *Immunological Reviews* **329**, e13438 (2025).

1234 83. J. H. Wang, E. L. Reinherz, The structural basis of alphabeta T-lineage immune
1235 recognition: TCR docking topologies, mechanotransduction, and co-receptor function.
1236 *Immunol Rev* **250**, 102–119 (2012).

1237 84. T. Sasada *et al.*, Involvement of the TCR Cβ FG Loop in Thymic Selection and T Cell
1238 Function. *Journal of Experimental Medicine* **195**, 1419–1431 (2002).

1239 85. M. Touma *et al.*, The TCR Cβ FG Loop Regulates αβ T Cell Development1. *The Journal*
1240 *of Immunology* **176**, 6812–6823 (2006).

1241 86. S. T. Kim *et al.*, TCR Mechanobiology: Torques and Tunable Structures Linked to Early
1242 T Cell Signaling. *Frontiers in Immunology* **3**, (2012).

1243 87. H. Li *et al.*, Lipid-regulated phosphorylation hierarchy of the T cell receptor tyrosine
1244 motifs. *Mol Cell* **85**, 3694–3710.e3698 (2025).

1245 88. W. W. Schamel, B. Alarcon, S. Minguet, The TCR is an allosterically regulated
1246 macromolecular machinery changing its conformation while working. *Immunological*
1247 *Reviews* **291**, 8–25 (2019).

1248 89. L. Kjer-Nielsen *et al.*, Crystal structure of the human T cell receptor CD3 epsilon gamma
1249 heterodimer complexed to the therapeutic mAb OKT3. *Proc Natl Acad Sci U S A* **101**,
1250 7675–7680 (2004).

1251 90. M. Arslan *et al.*, Effect of non-repetitive linker on in vitro and in vivo properties of an anti-
1252 VEGF scFv. *Scientific Reports* **12**, 5449 (2022).

1253 91. M. Krogsgaard *et al.*, Agonist/endogenous peptide-MHC heterodimers drive T cell
1254 activation and sensitivity. *Nature* **434**, 238–243 (2005).

1255 92. F. Letourneur, B. Malissen, Derivation of a T cell hybridoma variant deprived of functional
1256 T cell receptor alpha and beta chain transcripts reveals a nonfunctional alpha-mRNA of
1257 BW5147 origin. *Eur J Immunol* **19**, 2269–2274 (1989).

1258 93. W. Thomas *et al.*, Catch-bond model derived from allostery explains force-activated
1259 bacterial adhesion. *Biophys J* **90**, 753–764 (2006).

1260 94. C. D. Buckley *et al.*, Cell adhesion. The minimal cadherin-catenin complex binds to actin
1261 filaments under force. *Science* **346**, 1254211 (2014).

1262 95. D. L. Huang, N. A. Bax, C. D. Buckley, W. I. Weis, A. R. Dunn, Vinculin forms a
1263 directionally asymmetric catch bond with F-actin. *Science* **357**, 703–706 (2017).

1264 96. G. I. Bell, Models for the specific adhesion of cells to cells. *Science* **200**, 618–627 (1978).

1265 97. W. L. Jorgensen, J. Chandrasekhar, J. D. Madura, R. W. Impey, M. L. Klein, Comparison
1266 of Simple Potential Functions for Simulating Liquid Water. *J Chem Phys* **79**, 926–935
1267 (1983).

1268 98. B. Hess, C. Kutzner, D. van der Spoel, E. Lindahl, GROMACS 4: Algorithms for Highly
1269 Efficient, Load-Balanced, and Scalable Molecular Simulation. *J Chem Theory Comput* **4**,
1270 435–447 (2008).

1271 99. M. J. Abraham *et al.*, GROMACS: High performance molecular simulations through
1272 multi-level parallelism from laptops to supercomputers. *SoftwareX* **1-2**, 19–25 (2015).

1273 100. U. R. Shrestha *et al.*, Generation of the configurational ensemble of an intrinsically
1274 disordered protein from unbiased molecular dynamics simulation. *Proc Natl Acad Sci U S*
1275 *A* **116**, 20446–20452 (2019).

1276 101. K. Lindorff-Larsen *et al.*, Improved side-chain torsion potentials for the Amber ff99SB
1277 protein force field. *Proteins* **78**, 1950–1958 (2010).

102. F. Eisenhaber, P. Lijnzaad, P. Argos, C. Sander, M. Scharf, The double cubic lattice method: Efficient approaches to numerical integration of surface area and volume and to dot surface contouring of molecular assemblies. *J Comput Chem* **16**, 273–284 (1995).

103. R. Huey, G. M. Morris, A. J. Olson, D. S. Goodsell, A semiempirical free energy force field with charge-based desolvation. *Journal of Computational Chemistry* **28**, 1145–1152 (2007).

FIGURE LEGENDS

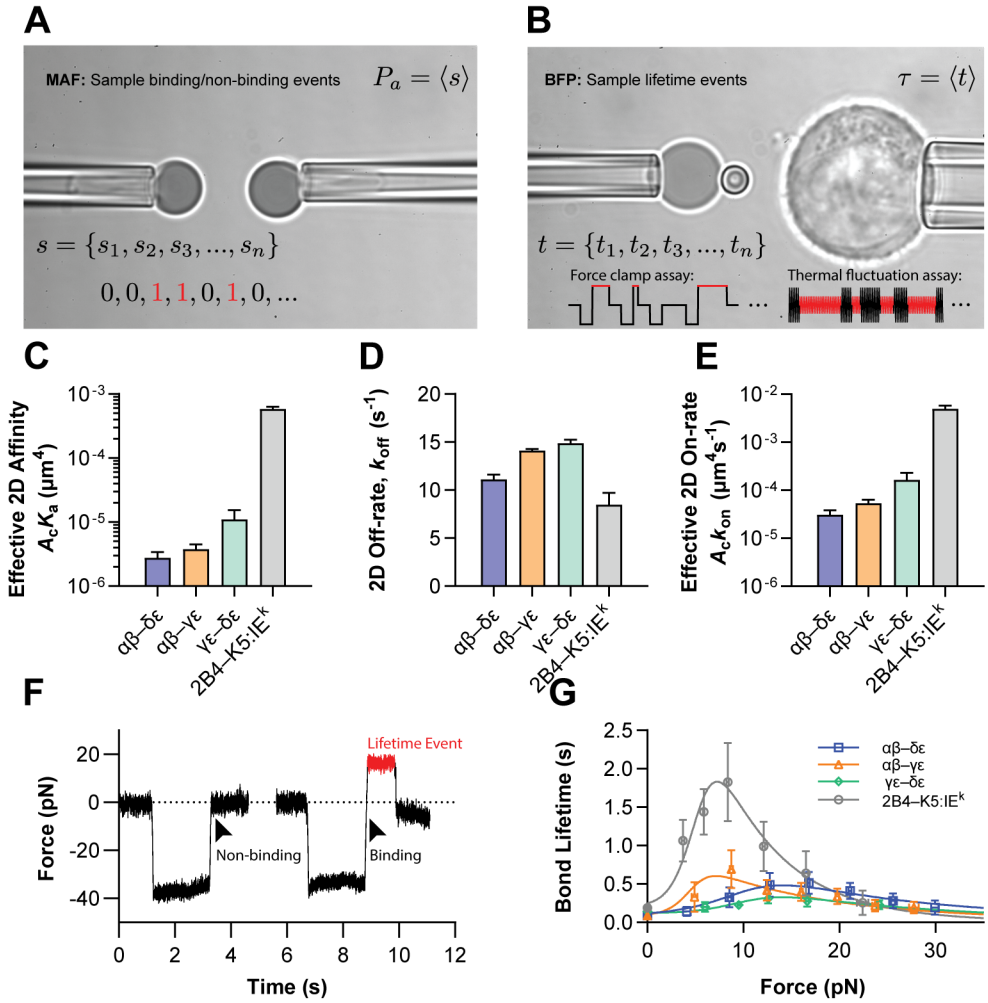

Figure 1. 2D kinetic quantifications of TCRαβ–CD3 ECD *cis*-interactions.
(A, B) Photomicrographs of the micropipette adhesion frequency (MAF) assay (*A*) and the biomembrane force probe (BFP) assay (*B*), overlain with legends indicating the measurement types. The two micropipettes held the probe (*left*) and the target (*right*), respectively, with each presenting one of the interacting pair. The target image shown in (*B*) is a hybridoma cell expressing full TCR–CD3 complexes, but beads coated with purified protein ECDs were also used, depending on the experiment. The target was brought into repeated contact with the probe to enable and interrogate ligand–receptor interactions. The probe, which was either a pressurized RBC (*A*) or a glass bead attached to the apex of the pressurized RBC (*B*), served a dual role of ligand presenter and force transducer, detecting the binding events to evaluate adhesion probability (*A*) and measuring bond lifetime (*B*), respectively, as indicated in the legends (see Methods). **(C)** Effective 2D affinities (A_cK_a) of pairwise *cis*-interactions between the ECDs of TCRαβ (αβ), CD3δε (δε), and CD3γε (γε) measured by MAF. **(D)** 2D off-rates (k_{off}) of the indicated *cis*-interactions quantified by the thermal fluctuation assay using BFP. **(E)** Calculated effective 2D on-rates ($A_ck_{on} = A_cK_a \times k_{off}$) of the indicated *cis*-interactions. Data are presented as mean ± SEM in (*C*)-(*E*), with the 2D affinity, off-

rate, and on-rate of the *trans*-interaction between cell-surface 2B4 TCR and its cognate pMHC K5:IE^k (*gray*) also plotted in the corresponding panels for comparison. **(F)** Representative force traces of non-binding *vs.* binding events from the BFP force-clamp assay. The target, either a bead or a cell, was driven to approach the probe (~ 0 pN before contact), pressed against it for 1 s (~ –35 pN), which resulted in either a non-binding (returning to ~ 0 pN) or a binding event (crossing 0 pN to a positive, tensile force) upon target retraction. The latter trajectory illustrates a lifetime event in which the ligand–receptor bond was clamped with a force of ~16 pN for ~0.5 s (*red*) until dissociation, indicated by a sudden drop in force to ~ 0 pN. **(G)** Force-dependent average lifetimes of pairwise αβ–δε, αβ–γε, and δε–γε *cis*-bonds (*points*, mean ± SEM of > 30 lifetime events per force bin) at zero force by thermal fluctuation assay (*closed symbols*) and at non-zero forces by force-clamp assay (*open symbols*). The overlaid smooth curves are the global fits of the two-state dissociation model (Supplementary Fig. 2; see Methods). In contrast to *cis*-bonds, the points and curve in *gray* denote the previously published force-lifetime results of the 2B4–K5:IE^k *trans*-interaction (*42*), which provides a direct comparison.

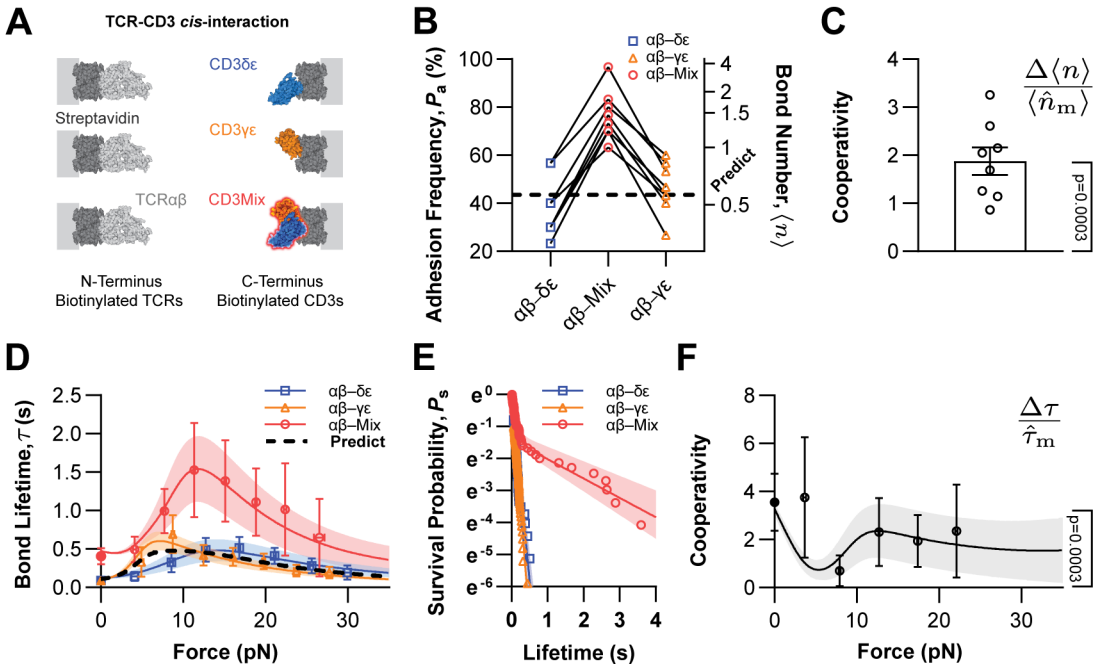

Figure 2. Experimental demonstration of cooperativity in *cis*-interaction of CD3γε, CD3δε, and TCRαβ ECDs.

(A) Experimental schemes. Purified protein ECDs were captured onto the RBC or bead surfaces through biotin-streptavidin (SA) coupling. N-terminally-biotinylated 2B4 hybrid TCRαβ was coated onto the probe (*left*), while C-terminally-biotinylated human CD3γε (*blue*), CD3δε (*orange*), or a 1:1 mixture of both (CD3m, *red*) was coupled onto the opposing target (*right*). These tail-to-head binding arrangements ensure preferred *cis*-interaction orientations for TCR–CD3 associations. **(B)** Adhesion frequency, P_a (*left ordinate*), and average bond number, $\langle n \rangle = -\ln(1 - P_a)$ (*right ordinate*), measured by the MAF assay. The same TCRαβ-bearing RBC was tested sequentially against three RBCs bearing, respectively, CD3γε, CD3δε, or CD3m in random order (*points connected by solid lines*). These CD3-bearing RBCs were from the same batch of streptavidinylated cells, which were then incubated with saturating amounts of CD3γε, CD3δε, and CD3m, respectively, to equalize site density coating. Each probe-target pair was tested for 30 cycles, with a 2-s contact time per cycle. The predicted bond number of dual-ligand RBCs (*dotted line*), $\langle \hat{n}_m \rangle$, is the sum of the bond numbers of TCRαβ interacting with CD3γε and CD3δε, separately. Thus, $\langle \hat{n}_m \rangle$ equals to the average of the bond numbers measured from the two RBCs bearing single CD3 species because the respective densities of CD3γε and CD3δε on the mixed ligand RBCs are half of the densities of CD3γε and CD3δε on the single-ligand RBCs under the assumption of concurrent and independent binding (see Methods). This no-cooperativity assumption is invalidated by the data, which clearly demonstrate that the actual measurements greatly outnumber the prediction (note that a log scale is used on the right ordinate). Several metrics were used to quantify cooperativity (*C*, *F*, and Fig. 3D, G), which is defined as the difference between the measurement and the prediction, normalized by the expected value assuming no cooperativity. **(C)** Positive 2D binding cooperativity of TCRαβ–CD3m *cis*-interaction.

Here, $\Delta\langle n_{\mathrm{m}}\rangle/\langle\hat{n}_{\mathrm{m}}\rangle$ (*points*) utilized the bond number in (*B*) as the cooperative metric. The case of no cooperation corresponds to a zero value, whereas a greater than zero value reveals 2D binding cooperativity. **(D)** Force-dependent average bond lifetime, $\tau(f)$, for TCRαβ–CD3m *cis*-interactions quantified using BFP. The predicted average bond lifetime of dual-species (*dotted line*), $\hat{\tau}_{\mathrm{m}}$, is the weighted sum of the single-species force-lifetime curves of the αβ–δε and αβ–γε bimolecular bonds (replotted from Fig. 1G for comparison). The weights are fractions of bond formation based on the 2D binding affinities of single-ligand *cis*-interactions (Fig. 1C) and corresponding amounts (1:1 ratio). The overlaid smooth curves are the global fits of the two-state, two-pathway dissociation models (Supplementary Fig. 2A-I; see Methods). **(E)** The bond survival probability for the TCRαβ–CD3m *cis*-interactions derived from zero-force individual bond lifetimes (whose average is $\tau(0)$) measured from the thermal fluctuation assay. The bond survival probability curves of the αβ–δε and αβ–γε bimolecular bonds are shown for comparison (using pairwise lifetime data in Fig. 1D). **(F)** Positive bond lifetime cooperativity of dual-ligand *cis*-interaction, $\Delta\tau/\hat{\tau}_{\mathrm{m}}$, using the bond lifetime in (*D*) as the cooperative metric. Again, the no cooperation case corresponds to a zero value, whereas a greater than zero value reveals cooperativity in force-dependent bond lifetime. In (*D*) and (*F*), data points are presented as mean ± SEM from > 30 lifetime-events per force bin; global-fitting force-lifetime and survival-probability curves (*D*, *E*, and *F*) are plotted with means (*solid line*) and standard deviations (*shaded area*). Significance in (*C*) and (*F*) was assessed using a one-sample t-test against zero.

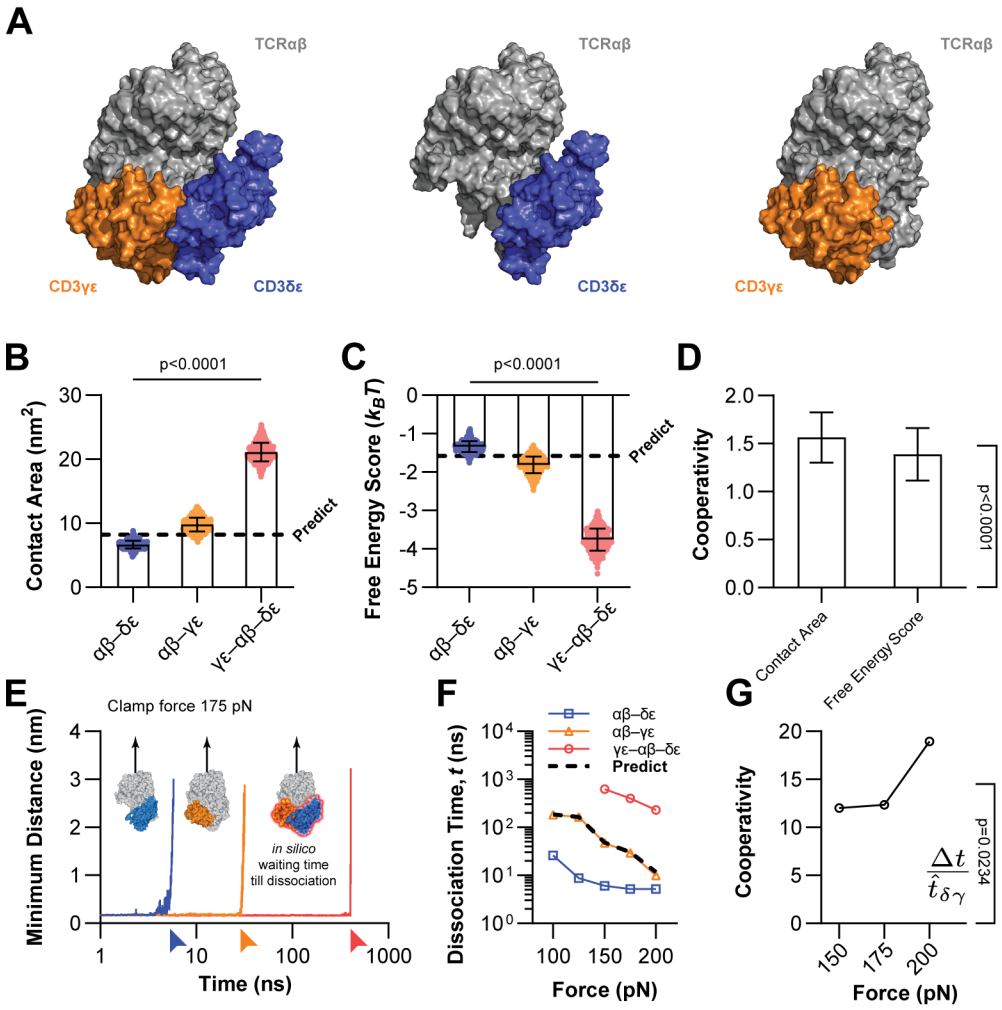

Figure 3. Computational demonstration of cooperativity in *cis*-interaction of CD3γε, CD3δε, and TCRαβ ECDs.

(A) Initial structures for MD simulations. The ECD of CD3γε–TCRαβ–CD3δε trimolecular complex (*left*) was modeled based on the published cryo-EM structure (*28*), 6JXR. The two TCRαβ–CD3δε (*middle*) and TCRαβ–CD3γε (*right*) bimolecular structures were obtained by removing CD3γε and CD3δε from the trimer, respectively. **(B, C)** Contact areas and interaction energies for the dimers and trimer from CMD simulations. Mean ± SD of contact areas (*B*), defined by solvent accessible surface areas (*101*), and interaction energies (*C*), quantified using empirical free energy scores (*102*), were calculated from the TCRαβ–CD3δε (*blue*), TCRαβ–CD3γε (*orange*), and CD3γε–TCRαβ–CD3δε (*red*) structures (Supplementary Fig. 3B, C). Statistics were obtained by comparing any two groups using unpaired t-tests. **(D)** Cooperative metrics of the δε–αβ–γε trimeric complex in terms of contact areas (*left*) and free energy scores (*right*). The cooperative analyses were conducted similarly to that in Fig. 2C, but were based on contact areas and interaction energies in (*B*) and (*C*) rather than on bond numbers. **(E)** The minimum distances between TCRαβ and corresponding CD3δε (*blue*), CD3γε (*orange*), or both (*red*) *vs.* simulation time, calculated from representative trajectories of SMD-simulated TCR–CD3 ECD dissociation.

Initial molecular constructs of αβ–δε and αβ–γε dimeric assemblies and of δε–αβ–γε trimeric complex are indicated, where TCRαβ N-termini were pulled away from corresponding C-terminal anchored CD3s during a 175-pN force-clamping SMD simulations (*insets*). The sudden rise of the trajectory from the baseline signifies the time point of dissociation (*arrows*). **(F)** *In silico* times required for the complex to dissociate, $t(f)$, under constant forces of 100-200 pN from SMD simulations. The predicted time-to-dissociation of the γε–αβ–δε trimer (*dotted line*), $\hat{t}_{\delta\gamma}$, is the TCR dissociation time from both δε and γε, under the assumption that the two bimolecular bonds are in parallel, and their dissociations are independent and concurrent (see Methods). **(G)** Cooperative metric $\Delta t/\hat{t}_{\delta\gamma}$ *vs.* force of the δε–αβ–γε trimeric complex. The cooperative analyses were conducted similarly to that in Fig. 2F but were based on the SMD simulated time-to-dissociation in (*F*) rather than on experimentally measured bond lifetimes. Significance was assessed using one-sample t-tests against zero in (*D*) and (*G*).

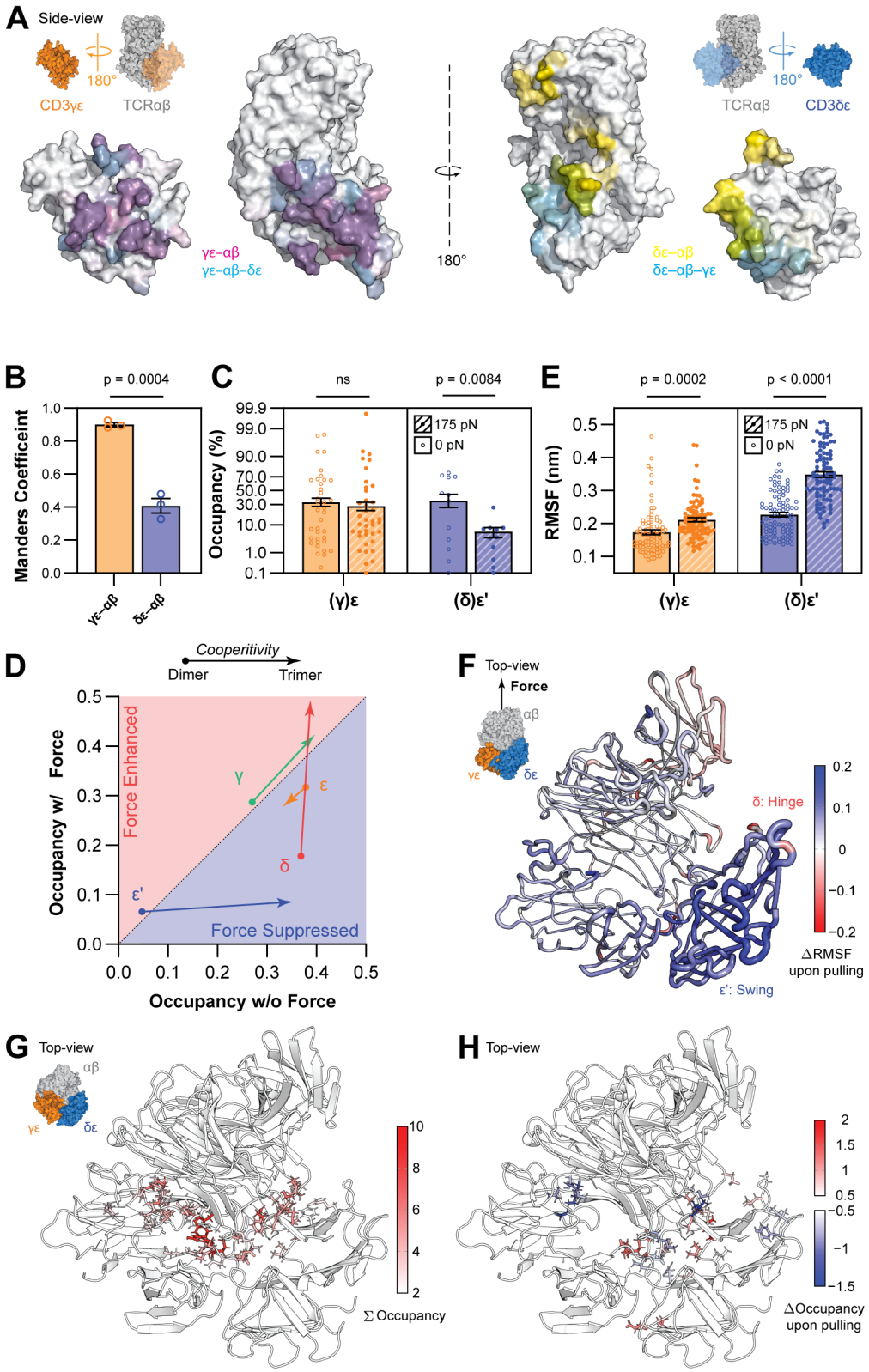
A
Side-view
CD3γε
TCRαβ
180°
γε–αβ
γε–αβ–δε
δε–αβ
δε–αβ–γε
TCRαβ
CD3δε
B
p = 0.0004
Manders Coefficeint
γε–αβ
δε–αβ
C
ns
p = 0.0084
Occupancy (%)
175 pN
0 pN
(γ)ε
(δ)ε'
E
p = 0.0002
p < 0.0001
RMSF (nm)
D
Cooperitivity
Dimer
Trimer
Force Enhanced
Force Suppressed
Occupancy w/ Force
Occupancy w/o Force
F
Top-view
Force
δ: Hinge
ε': Swing
ΔRMSF upon pulling
G
Top-view
Σ Occupancy
H
Top-view
ΔOccupancy upon pulling

Figure 4. Structural basis of force-dependent cooperative TCR–CD3 ECD *cis*-interactions.

(A) Dynamic "footprints" of αβ–γε (*left*) and αβ–δε (*right*) interfaces are defined by the CMD-derived occupancies, which were projected onto the light gray space-filling representations of TCR–CD3 ECDs. The *insets* depict the placements and orientations of γε (*orange*) and αβ–δε (*gray*), αβ–γε (*gray*) and δε (*blue*) from the far left to the far right: two sets of side-view images mirroring each other to allow CD3s to face outward. The respective γε (*left*) and δε (*right*) binding interfaces with αβ are exposed by flipping the CD3s 180° while keeping the rest fixed (before *transparent*; after *opaque*). The pseudo-color maps are coded for interface footprints in the trimer (*cyan*; only the unobscured areas are visible) as well as in dimers with γε (*magenta*) and δε (*yellow*), with intensity levels matching the occupancy values, ranging from 0% (white) to 100% (fully saturated). When comparing trimer *vs.* dimer, the unobscured *cyan* areas relative to the *magenta* and *yellow* areas represent the increased footprints of αβ with γε (*left two* panels) or δε (*right two* panels) from dimer structures upon assembly of the trimer structure by incorporating the missing CD3. When comparing γε *vs.* δε, the magenta area is larger than the yellow area, indicating a more stable αβ–γε than αβ–δε dimer. Moreover, the overlapping areas are smaller on the right (*cyan* + *magenta*) than on the left (*cyan* + *yellow*), both in absolute values and percentages, indicating smaller cooperative effects due to adding δε to αβ–γε than adding γε to αβ–δε in the trimer and demonstrating asymmetry with less contact adjustment of γε than δε after trimer assembly. **(B)** Quantification of colocalization of occupancies between trimer and dimers by Manders' overlap coefficient, defined by $\sum D_i T_i / (\sum D_i^2 \sum T_i^2)^{1/2}$ where *i* denotes the residue index of αβ–γε (*orange*) and αβ–δε (*blue*); D_i and T_i denote the ith occupancy values of dimer and trimer, respectively, before and after *cis*-cooperative trimer assembly with the missing CD3. A Student t-test was used to assess significance based on three independent simulation repeats. **(C)** Interfacial stabilities of two ε-chains under 0 and 175 pN force, quantified by mean ± SEM of ε (*left*) or ε' (*right*) chains residues with non-zero occupancies (*points*) interacting with αβ calculated from CMD (0 pN, *open bars*) or SMD (175 pN, *hatched bars*) simulated γε–αβ–δε trimeric structure. Here, γ-associated ε-chain (ε) and δ-associated ε-chain (ε') are distinguished using the prime superscript. **(D)** Mean occupancies of γ (*green*), ε (*orange*), δ (*red*), or ε' (*blue*) chains interacting with αβ quantified by averaging non-zero occupancies calculated from CMD (without force, *x*-axis) or SMD (with force, *y*-axis) simulated αβ–γε and αβ–δε dimer structures (*arrow starting points*) or γε–αβ–δε trimer structure (*arrow ending points*). **(E)** Fluctuations of two ε-chains under 0 and 175 pN force, quantified by mean ± SEM of residue RMSFs of ε (*left*) or ε' (*right*) chains calculated from CMD (0 pN, *open bars*) or SMD (175 pN, *hatched bars*) simulated γε–αβ–δε trimeric structure. **(F)** Change of flexibilities in the TCR–CD3 complex upon pulling. The *inset* shows the top view of the γε–αβ–δε ECD structure under a 175 pN force. Differential RMSF profiles between SMD and CMD (*blue* for enhanced and *red* for suppressed fluctuations) are mapped onto the ribbon view of trimeric ECD. The residues' absolute ΔRMSF values are represented by the thickness of the protein backbone. Statistical significance levels were assessed by Welch's t-test assuming non-equivalent SD. **(G, H)** Critical interacting residues mapped onto the γε–αβ–δε interfaces showing the strong-interacting (*G*) and the force-sensitive (*H*) contacts.

The *inset* in (*G*) is the top-view of the γε–αβ–δε ECD structure. The same top-views of the full ECD assembly are shown in ribbon representation where tightly interacting residues are highlighted by sticks and colors. Only strong-interacting contact residues are shown in (*G*) using sidechains colored from *white* to *red*, based on their ΣOccupancy level. The force-sensitive residues with significant occupancy differences upon applying a 175 pN clamping force are shown in (*H*), with sidechains colored from *white* to *red* for increases and from *white* to *blue* for decreases in their ΔOccupancy level (see Methods).

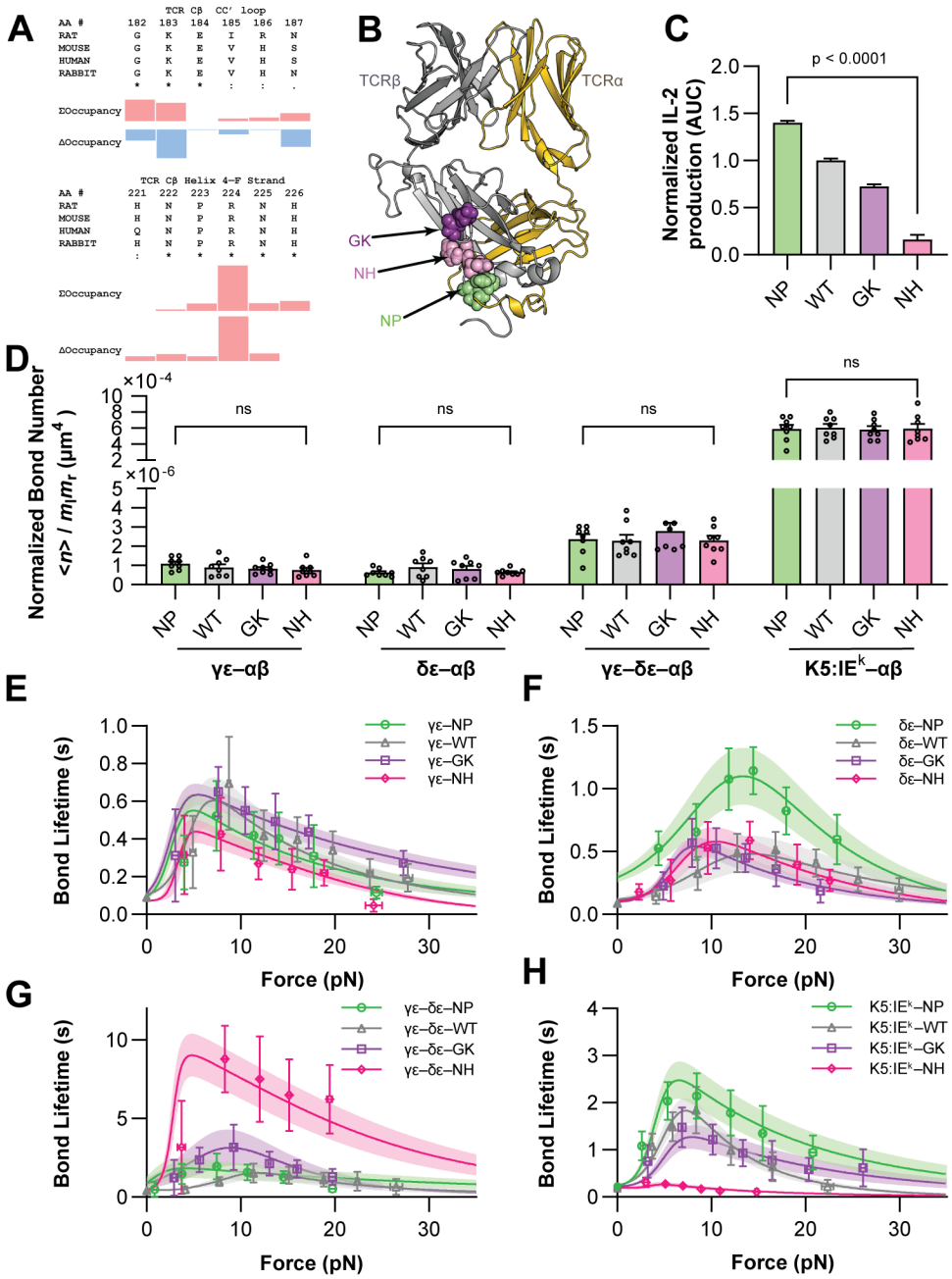

Figure 5. Effects of mutating Cβ contacting residues on *cis*-interaction affinity and bond lifetime.

(A) TCRβ local segments with distinct force-responses. Residues in the CC' loop (*upper table*) and Helix 4 – F strand (*lower table*) of the Cβ domain both contact CD3 (indicated by ΣOccupancy) but respond differently to 175 pN clamping force (indicated by ΔOccupancy). **(B)** TCRαβ structure with double-mutants listed in (*A*) highlighted on the Cβ CC' loop and Helix 4-F strand, which contribute to the force-dependent cooperative TCR–CD3 *cis*-interaction according to (*A*). **(C)** Differential IL-2 cytokine productions of cells containing Cβ mutations. The hybridoma

expressing 2B4 TCR WT and MTs were stimulated by K5:IE^k displayed on CHO cells. The area under the dose-response curve (AUC), normalized by that of WT, quantifies the relative IL-2 secretion. This data has previously been reported (*26*) and is reformulated here to facilitate experimental design and correlative analysis. **(D)** Normalized average number of bonds of *cis*-interactions between CD3δε (*first group*), CD3γε (*second group*), or CD3δε–CD3γε (*third group*) and TCRαβ WT (*gray*) or β-chain double-mutants NP (*green*), GK (*purple*), or NH (*magenta*) MTs. Corresponding $\langle n \rangle / m_{\mathrm{l}} m_{\mathrm{r}}$ of WT and indicated mutant 2B4 TCRs on hybridomas *trans*-interacting with K5:I-E^k are plotted for comparison (*fourth group*). **(E-G)** Force-dependent bond lifetimes (*points*, mean ± SEM of > 30 lifetime events per force bin; *curves with shades*, mean ± SD of globally fitted bond profiles) of *cis*-interactions of CD3γε (*E*), CD3δε (*F*), or both (*G*) with TCRαβ WT (*gray*), NP (*green*), GK (*purple*), or NH (*magenta*) MTs. **(H)** Corresponding $\tau(f)$ of WT and indicated mutant 2B4 TCRs on hybridomas *trans*-interacting with K5:I-E^k are shown for comparison. This data has previously been reported (*42*) and is replotted here to facilitate correlative analysis and mechanistic understanding.

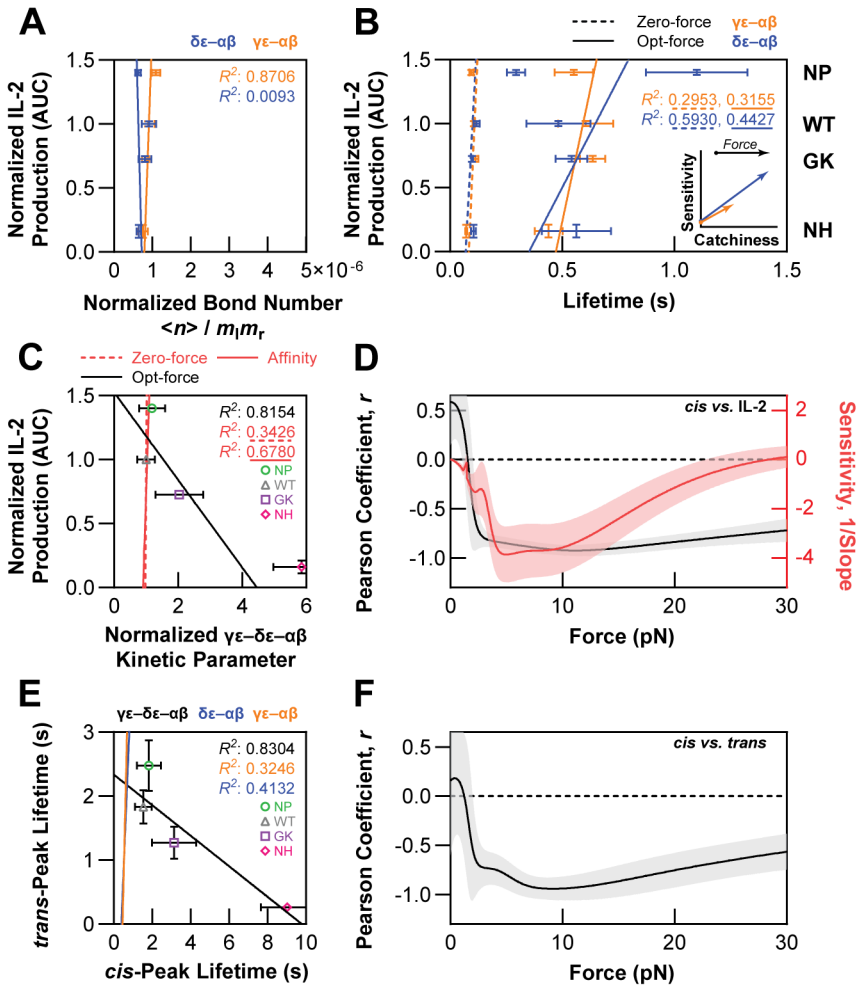

Figure 6. Correlating ECD *cis*-interaction parameters of TCRαβ with CD3γε, CD3δε, or both with T cell function and *trans*-interaction parameters between TCR and pMHC.

(A) The correlations between the IL-2 secretion (in Fig. 5C) and effective 2D affinity for αβ–γε (*orange*) or αβ–δε (*blue*) *cis*-interaction (in Fig. 4C, *first* and *second group*). **(B)** The correlations between IL-2 secretion and zero-force (*dotted lines*) *vs.* optimal-force (*solid lines*) bond lifetime for αβ–γε (*orange*) or αβ–δε (*blue*) *cis*-interaction (in Fig. 5E, F). *Inset*: Different catchiness and sensitivity of CD3γε (*orange*) *vs.* CD3δε (*blue*). The arrows display the effects of force. (**C**) Correlations between normalized γε–δε–αβ *cis*-kinetics and T-cell signal. The mean ± SEMs of relative IL-2 AUC (in Fig. 5C) are negatively correlated with the peak lifetimes of ECD *cis*-interactions of WT and MT TCRαβs (in Fig. 5G) when both CD3γε, CD3δε co-presented (*black*). The poor correlations between IL-2 production and zero-force bond lifetime (*red dashed line*) or normalized number of bonds (*red solid line*) for γε–δε–αβ *cis*-interactions are also plotted for comparison. **(D)** Goodness-of-fit and sensitivity of force-dependent bond lifetimes of γε–δε *cis*-interacting with WT and MT TCRαβs in predicting downstream IL-2 responses. The Pearson correlation coefficients (*black*) and inverse of the linear-regression slopes (*red*) between

normalized IL-2 AUC and γε–δε–αβ *cis*-catch bonds are plotted for a range of forces (*curves with shades*, mean ± SD). (**E**) Correlations between γε–δε–αβ *cis*- and *trans*-bond lifetimes. The mean ± SEMs of the peak lifetimes of trimolecular *cis*-interactions (in Fig. 5G) are negatively correlated with those of *trans*-interactions from WT and MT 2B4 TCRs expressed on hybridoma cells interacting with K5:IE^k (in Fig. 5H). The poor correlations between the peak lifetimes of bimolecular *cis*-interactions (*orange*, αβ–γε and *blue*, αβ–δε) with the peak lifetimes of the WT and MT 2B4 TCRs *trans*-interacting with K5:IE^k are plotted for comparison (in Fig. 5E, F). (**F**) Anti-correlation between the γε–δε–αβ *cis*-interaction and the TCR–pMHC *trans*-interaction for WT and MT. The Pearson correlation coefficients of the *cis*- *vs. trans*-bond lifetime are shown for every single magnitude of force (*curves with shades*, mean ± SD).